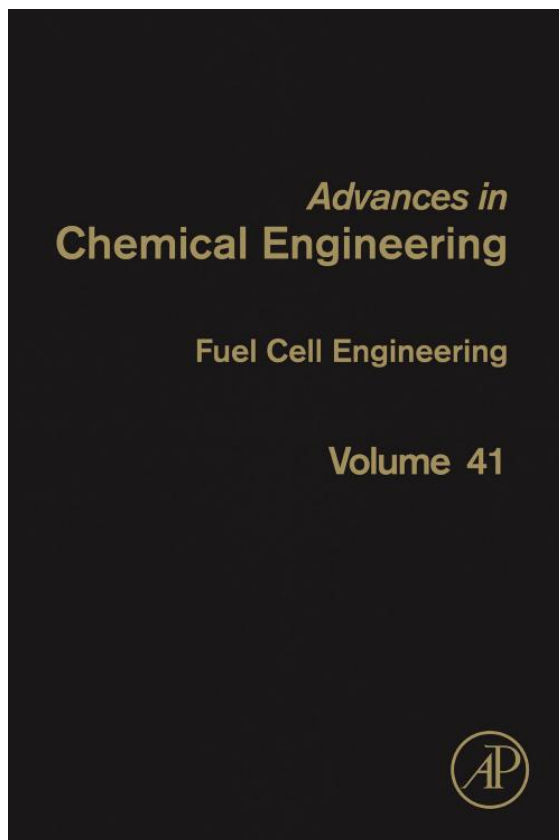


**Provided for non-commercial research and educational use only.
Not for reproduction, distribution or commercial use.**

This chapter was originally published in the book *Advances in Chemical Engineering*, Vol. 41 published by Elsevier, and the attached copy is provided by Elsevier for the author's benefit and for the benefit of the author's institution, for non-commercial research and educational use including without limitation use in instruction at your institution, sending it to specific colleagues who know you, and providing a copy to your institution's administrator.



All other uses, reproduction and distribution, including without limitation commercial reprints, selling or licensing copies or access, or posting on open internet sites, your personal or institution's website or repository, are prohibited. For exceptions, permission may be sought for such use through Elsevier's permissions site at:

<http://www.elsevier.com/locate/permissionusematerial>

From: Robert J. Braun, Tyrone L. Vincent, Huayang Zhu, and Robert J. Kee,
Analysis, Optimization, and Control of Solid-Oxide Fuel Cell Systems.
In Kai Sundmacher, editor: *Advances in Chemical Engineering*, Vol. 41,
Burlington: Academic Press, 2012, pp. 383-446.

ISBN: 978-0-12-386874-9

© Copyright 2012 Elsevier Inc.
Academic Press

CHAPTER 7

Analysis, Optimization, and Control of Solid-Oxide Fuel Cell Systems

Robert J. Braun,^{1,*} Tyrone L. Vincent,² Huayang Zhu,¹ and Robert J. Kee¹

Contents		
	1. Introduction	384
	2. Steady-State SOFC Stack and System Modeling	387
	2.1 Process overview	388
	2.2 SOFC stacks	389
	2.3 Heat exchangers and catalytic reactors	391
	2.4 System-level models	393
	2.5 System thermal modeling	395
	2.6 Fuel processing considerations	401
	3. Analysis of SOFC Systems	406
	3.1 Performance definitions	407
	3.2 Operating characteristics	408
	3.3 Exergy analysis	415
	4. Technoeconomic Modeling and Optimization of SOFC Systems	422
	4.1 Life cycle costing	422
	4.2 Optimal parameter selection	425
	5. Process Control	429
	5.1 Physical constraints	430
	5.2 Inputs and outputs	430

¹Department of Mechanical Engineering, College of Engineering and Computational Sciences, Colorado School of Mines, Golden, Colorado, USA

²Department of Electrical Engineering and Computer Science, College of Engineering and Computational Sciences, Colorado School of Mines, Golden, Colorado, USA

* Corresponding author, E-mail address: rbraun@mines.edu

5.3 Effect of dynamics	431
5.4 Model-predictive control	436
6. Summary and Conclusions	442
References	443

Abstract

This chapter discusses solid-oxide fuel cells at the system level and the integration of the cell stack with balance-of-plant components. Balance-of-plant components includes fuel processors (e.g., desulfurization and fuel reforming), pumps and blowers, heat exchangers, and catalytic reactors. Understanding and predicting thermal and chemical communication among these components are essential elements of system design and control. System analysis considers overall efficiency of converting fuel to electricity as well as combined heat and power (CHP) applications that beneficially use waste heat. In addition to conversion efficiency alone, analysis of life-cycle cost (LCC) plays an important role in optimizing system performance. The chapter concludes with a discussion of model-predictive control (MPC), wherein physically based models can be incorporated into real-time process-control strategies.

1. INTRODUCTION

Development of solid-oxide fuel cell (SOFC) systems is proceeding at power-generation scales ranging from 50 W to 500 MW. The high operating temperature and solid state electrolyte produce attractive benefits for a variety of applications, including portable (50–1000 W), mobile (500 W–20 kW), stationary residential and commercial (1 kW–1 MW), industrial (1–5 MW), and central utility (>100 MW) power systems. Research, design, and development activities for mobile SOFC systems encompass air-independent, unmanned undersea vehicles (UUVs; [Braun and Kattke, 2011](#); [Burke and Carreiro, 2006](#)), unmanned aerial vehicles ([Erikstrup et al., 2009](#); [Himansu et al., 2006](#); [Miller and Reitz, 2010](#); [Sun et al., 2009](#)), auxiliary power units in the transportation sector ([Braun et al., 2009](#); [Mukerjee et al., 2009](#)), and even railway locomotives ([Schroeder and Majumdar, 2009](#)). Most development activity concentrates on stationary power, including combined heat and power (CHP) applications ([Braun, 2010](#); [Braun et al., 2006](#); [Colella et al., 2010a,b](#); [Colson and Nehrir, 2011](#); [Hawkes et al., 2007, 2009](#); [Kazempoor et al., 2011](#); [Nanaeda et al., 2010](#); [Verda and Quaglia, 2008](#)), integrated coal gasification-SOFC systems ([Braun et al., 2012](#); [Liese, 2010](#); [Verma et al., 2006](#)), and SOFC-gas turbine hybrids fueled from natural gas ([Costamagna et al., 2001](#); [Massardo and Lubelli, 2000](#);

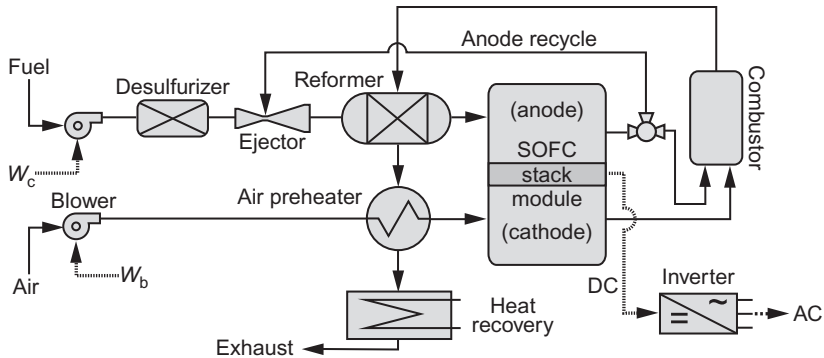


Figure 1 Generic SOFC system employing anode gas recycle.

Mueller *et al.*, 2008; Yang *et al.*, 2007). The often stated advantages of SOFC technology include high efficiency, fuel flexibility, high-grade waste heat for bottoming-cycle integration or cogeneration, low chemical emissions, power scalability, and the potential for low unit costs when mature.

Figure 1 illustrates a generic SOFC system, incorporating anode gas recycle (AGR) and waste-heat recovery. The basic components of an SOFC power plant consist of a fuel processor, fuel-cell power module, power-conditioning equipment for DC-to-AC inversion, and process-gas heat exchangers. Because of their high operating temperature, SOFCs produce varying grades of waste heat that can be recovered for process heating, power augmentation via an expander, or exported for cogeneration (or trigeneration) purposes. Beneficially using waste heat significantly impacts system efficiency, economics, and environmental emissions. Thus, a physically based understanding of the interactions among unit processes is necessary for designing systems that maximize the potential benefits of SOFCs for both electrical energy generation and thermal energy utilization.

Despite these advantages and much recent progress, SOFC technology faces numerous challenges before commercially viable systems are widely available. In traditional power-generation systems, a load step of 20–25% of the generator rating is considered large, causing significant transients (Lassiter, 1998). Distributed power systems, such as in mobile or commercial building applications, may require load steps of 50–60% of system rating without causing safety or stability problems. Load step changes of this magnitude may take several minutes or longer for fuel-cell systems due to the thermal lag of the fuel cell and fuel-processing hardware.

Understanding SOFC dynamic response to operational transients and perturbations is important in system control. The fuel cell may set its operating point based on a control signal from the inverter. The time

constant of an SOFC can be 30 s or more (Achenbach, 1995; Huang *et al.*, 2011). This behavior translates into an approximate time of 2–5 min for the operating point of the fuel cell to increase or decrease from the old value to the new value set by the control signal (Achenbach, 1995; Aguiar *et al.*, 2005; Colclasure *et al.*, 2011).¹ Thus, the cell temperature dynamics are on the order of hundreds of seconds and given the numerous temperature dependent performance characteristics, they affect all other state variable dynamics. During this transient, if the power demanded by the inverter is not matched by the power output from the fuel cell, there will be a power deficiency or an excess. In the case of a call for power, an increase in current results in a decrease in cell voltage; simultaneously, an excess production of oxygen anions (O^{2-}) occurs at the cathode. Changes in power demand can occur on millisecond timescales in many applications. Fast load dynamics present challenges to SOFC systems where the thermal response of the cell stack and supply of fuel and air cannot follow such fast perturbations.² Control of reactant supply during large load steps is particularly important as the oxygen anions that migrate across the solid electrolyte are likely to arrive at the anode where no fuel is available for oxidation. When such a loss of fuel supply occurs, these highly reactive anions can then oxidize the nickel in the anode cermet, damaging the cell.

Issues of safe operation and control also exist when stepping *down* in load. During this transient, excessive unreacted fuel can exit the fuel-cell stack for a short period of time and enter the tail-gas combustor. Depending upon how the fuel-cell stack is thermally integrated with the combustor, the subsequent fuel oxidation and heat release may generate large temperature gradients in the fuel-cell components and downstream heat exchangers, causing high thermal stresses or otherwise exceeding temperature limits. In the case of a decrease in power demand, that is, when the current demand is less than the available current, unoxidized fuel will exit the cell, reducing the system efficiency. There are additional concerns for loss in electric load beyond the concomitant inefficiency. Excess fuel can cause large heat release in the catalytic combustor, which is positioned downstream of the fuel-cell stack. High-temperature excursions can damage the combustion catalyst via sintering. Safety concerns associated with sudden load loss are proportional to both the magnitude and duration of the load excursion.

Fuel processing and thermal management are also critical to the performance of all types of fuel cells. Proper steam-to-carbon (SC) ratios in

¹ The time to steady state may be even longer during load changes because control is complicated by changes in fuel cell efficiency.

² Although not discussed in this chapter, hybridization with energy-storage components (e.g., secondary batteries or supercapacitors) is often an important element of achieving aggressive load-following demands.

the fuel reformer feedstock must be maintained during these operational changes to eliminate harmful carbon deposition in either reformer or fuel-cell stack components. Such operational considerations must be resolved with an understanding of the system dynamics, leading to effective control strategies.

The purpose of model development is to meet specific design or simulation objectives with adequate precision. For example, models that are developed to support design optimization can be quite different from models that are intended to support process control. As a practical matter in most multiphysics multiscale modeling, models are based upon approximations that are commensurate with the objectives. It is often necessary to bridge greatly disparate time and length scales. For instance, it is usually impractical to incorporate the detailed nano- and microstructure of a composite electrode into the model of even a single tube or channel. Rather, effective transport properties (e.g., diffusion coefficients) are derived from fine-scale models that can be used at larger length scales. A fuel-cell stack may be composed of hundreds, or thousands, of small channels. It may be appropriate to assume that all the individual channels behave similarly, or at least that a few sampled channels can be used to represent groups of channels.

This chapter focuses on the modeling, analysis, optimization, and control of SOFC-based energy systems. Modeling approaches for the fuel-cell stack, heat exchangers, and the integrated system are presented. The presentation has a predominately system design focus (as opposed to off-design system simulation) and includes discussion of system-level operating characteristics, thermal modeling, exergy analysis, life-cycle cost (LCC) minimization, and control. Chapter content is constrained to nonhybridized SOFC systems, that is, those systems that have not been integrated with gas turbines or other prime movers.

2. STEADY-STATE SOFC STACK AND SYSTEM MODELING

System-level models are typically a collection of component models that are integrated such that input and output variables are exchanged between components and whose performance metrics may be interrelated. The mathematical description of the system is formulated in terms of governing equations that are established from (1) conservation laws, (2) thermophysical property relationships, (3) component performance characteristics, and (4) interface and boundary conditions. Examples of component performance characteristics include blower, compressor and power-conditioning efficiencies, fuel-cell polarization curves, and heat-exchanger effectiveness. The equations for

mass and energy balances, property relationships, and performance characteristics form a set of nonlinear-coupled equations incorporating design and operating variables. This section begins with an overview of system operation, motivating subsequent discussions on system analysis and optimization.

2.1 Process overview

Despite its fuel flexibility, robust operation of the SOFC stack is most easily accomplished when the fuel mixture entering the stack contains a large fraction of hydrogen. As illustrated in [Figure 1](#), natural gas entering the plant is pressurized, stripped of sulfur, and mixed with superheated steam via recycle of depleted anode exhaust gases. The fuel-steam mixture is delivered to an integrated fuel processor, combining the functions of fuel heating and steam reforming. The thermal energy required to support the endothermic reforming reactions is supplied by the hot exhaust gases leaving the catalytic tail-gas combustor. The resulting hydrogen-rich fuel gas is directed into the anode compartments of the individual cells within the stack through a flow-distribution manifold. Within the cells, the fuel stream is transported through the porous composite anode where heterogeneous reactions at the anode-gas-electrolyte interfaces electrochemically oxidize the fuel. The rate of electrochemical fuel oxidation varies spatially within the anode, with the rate being a function of the local current density. Analogous to the fuel delivery, fresh air is supplied with an air blower or compressor, preheated, and delivered to the cathode compartment of the SOFC stack. It is typical to provide air in excess of the stoichiometric requirements of the electrochemical oxidation of the fuel stream. Excess air ranges from 100% to 600% and is used to maintain a desired cell operating temperature. An inverter converts direct current (DC) from the SOFC to alternating current (AC), a portion of which is used to service parasitic loads, such as the fuel compressor and air blower (e.g., W_c and W_b , respectively).

Not all the fuel delivered to the cell stack is consumed to avoid generating an unacceptably low stack voltage and thereby damage cell integrity. Fuel utilization measures the fraction of fuel that is electrochemically oxidized. SOFC stacks typically operate with fuel utilization in the range of 70–85%. Recycle of the anode exhaust gases alters the amount of fuel utilized in the cell stack and hence the stack efficiency. Oxidation of unspent fuel exiting the anode is accomplished in a tail-gas combustor. Because the fuel leaving the SOFC is highly diluted with reaction products (i.e., H_2O and CO_2), the oxidation must usually be accomplished via heterogeneous reaction over an active catalyst (e.g., rhodium). Products of the catalytic tail-gas combustion process are then recovered for use in fuel

processing and air preheating before being made available for external heat recovery in the form of hot water, steam, or warm air.

The addition of the fuel-processing equipment adds complexity, capital cost, maintenance, and inefficiency to the system. Nonetheless, this equipment is necessary in any practical system operating on readily available hydrocarbon fuels. Because overall system efficiency depends upon the efficiency of hydrogen production, design of the fuel reforming processes plays a major role in the optimal design and operation of the system. SOFC systems that are fueled with natural gas or other hydrocarbon-based fuels usually employ a combination of internal and external reforming (ER) methods. The required steam may be supplied either by a waste-heat boiler (Braun *et al.*, 2006) or by recycled fuel-cell reaction products (Figure 1 illustrates anode recycling). Other hydrogen-production processes, such as catalytic partial oxidation (CPOX) or autothermal reforming (ATR), are also available. Choosing the fuel reforming process for particular applications depends on fuel type, cost, efficiency, transient response, and technology readiness. Additional process-design considerations, such as cathode gas recycle, separate air and fuel gas circuits, fan and compressor selection, etc., are also viable options to be evaluated in design trade studies (Autissier *et al.*, 2007; Braun, 2010).

There are several alternative approaches for recovering thermal energy from fuel-cell exhaust gases. The temperature of the useful waste-heat product depends on where the heat is extracted in the system. As illustrated in Figure 1, heat extraction immediately downstream of the combustor produces the highest grade of heat, whereas heat recuperation after the air preheater will produce the lowest grade of heat, although this is more than sufficient for producing domestic hot water. In addition to the application requirements, another consideration for heat extraction design is that high-temperature heat recuperation can lower temperature differences in the downstream heat exchangers, thereby increasing their size and the associated capital cost (Rienschke *et al.*, 1998a).

2.2 SOFC stacks

For the purposes of stack design and optimization, three-dimensional representations of flow and heat transfer are usually very important. For example, inlet and exhaust manifolds must be designed such that fuel and air flow are distributed uniformly among all channels. However, there are often competing objectives. Flow uniformity can be realized with small channel dimensions but at the expense of high pressure drop. Large pressure drops significantly reduce overall efficiency because of the increased parasitic power needed to drive blowers. Achieving spatially uniform temperatures is usually an important aspect of stack

design. Because chemistry depends strongly on temperature, achieving uniform temperature enables all cells to operate at their peak performance. Additionally, large temperature gradients can cause damage, or failure, in critical ceramic components and seals.

Large-scale computational fluid dynamics (CFD) software can be a powerful tool in assisting stack design and development. Such models can handle great geometric complexity, including high-level user interfaces for geometry definition and meshing. Although CFD models provide sophisticated fluid flow and heat-transfer capabilities, they are usually limited in their ability to represent complex chemistry and electrochemistry. In the case of commercial software, the user has, at best, restricted access to the source code. Nevertheless, it is usually possible, and often necessary, to augment CFD software with special-purpose software to handle aspects of electrochemical phenomena.

Figure 2 shows a representative result from a large-scale three-dimensional model of a tubular stack (Kattke and Braun, 2011a; Kattke et al., 2011). This model integrates a three-dimensional CFD representation of the cathode air flow around the outsides of the tubes with electrochemistry models within each tube (Colclasure et al., 2011). The tubular fuel-cell model represents fuel flow and methane reforming chemistry within the anode-supported tubes, porous-media transport within the electrode structures, electrochemical charge transfer, and thermal balances. However, to

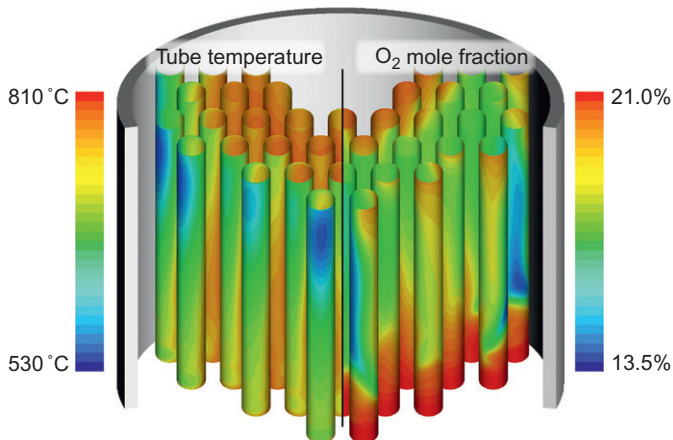


Figure 2 Modeling results of a 66-tube SOFC stack operating on a mixture of H_2 , CO , and CH_4 . The left-side tubes show tube surface temperatures and the right-side tubes show gas-phase oxygen mole fraction on the tube surfaces.

make the computation times reasonable, a number of approximations are made. The fuel flow is modeled using plug-flow approximations, neglecting radial gradients. The reforming chemistry is modeled with two global reactions (steam reforming and water-gas shift). The reactive porous-media transport within the composite electrodes is represented with only two computational cells. The tube wall temperature is assumed to be uniform through its thickness, but varying axially. The electrochemistry is represented in terms of a Nernst potential and various overpotentials. Although these approximations are certainly reasonable, it should also be recognized that more sophisticated models are available.

The tubular fuel-cell models in [Figure 2](#) cannot stand alone; they must be coupled with the external cathode air. Moreover, there is significant radiative and convective heat transfer between the tubes and the external shell. An iterative algorithm is developed to couple the complex three-dimensional flow and heat transfer outside the tubes with the complex chemistry and electrochemistry within the tubes. The external air flow and heat transfer are modeled with FLUENT ([Fluent software package](#)), and iterative coupling with the SOFC tubes is handled with a so-called user defined function (UDF).

The iterative algorithm must establish communication between the CFD model and the SOFC tube models, which have very different computational mesh structures ([Kattke et al., 2011](#)). The tubular fuel-cell models are solved using axial profiles of temperature and oxygen concentration supplied by the CFD model. The fuel-cell model predicts axial profiles of heat and oxygen fluxes, which are then used as boundary conditions by the CFD model for a subsequent iteration. The iterative process continues until convergence, usually in only a few iterations.

The design shown in [Figure 2](#) shows significant variations in local temperature and oxygen concentrations, within individual tubes and between tubes. The model-based design objective is to improve cell uniformity, and hence overall stack performance, by exploring alternative stack configurations and operating conditions.

2.3 Heat exchangers and catalytic reactors

Analogous to SOFC stack design, the model-based design process also beneficially impacts the development of heat exchangers and catalytic reactors. [Figure 3](#) illustrates the results of a three-dimensional simulation of a microchannel reformer that closely couples heat-exchanger and reformer functions. The exploded image on the left shows the internal manifold and channel structure for four layers of the reactor ([Kee et al.,](#)

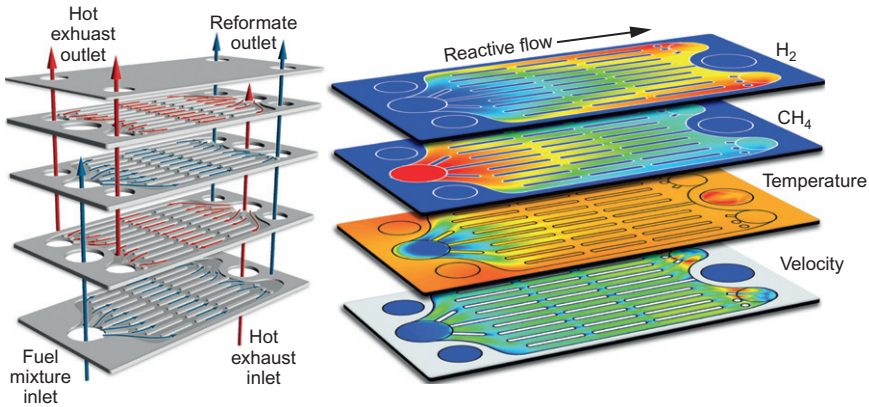


Figure 3 A microchannel reactor that closely couples the catalytic reforming function with the thermal control function.

2011). A reforming catalyst is loaded into alternate channel layers. In these layers, a fuel-steam mixture flows, with hot exhaust gases flowing through the noncatalytic channels. The reformer shown schematically in Figure 1 could use such a design. The contour maps on the right show predictions of selected concentrations, temperature, and velocity. This model considers both reactive fluid flow and coupled heat transfer in the reactor body.

As with fuel-cell stacks, models can assist design development that maximizes performance. In addition to reforming *per se*, a well-designed reactor should minimize pressure drop yet still achieve good flow uniformity among all channels and layers. Three-dimensional simulations (e.g., Figure 3) are valuable, but computation time can be long, especially when detailed catalytic chemistry is included.

Design of channel-manifold configurations is important in planar fuel-cell stacks, particularly for achieving flow uniformity with minimal pressure drop. This topic is also important in heat-exchanger design, with general design procedures being reasonably well established (Kays and London, 1998; Shah and Sekulić, 2003). Special-purpose models have been developed to provide channel-manifold design guidelines, with attention to fuel-cell applications (Costamagna *et al.*, 1994; Kee *et al.*, 2002; Wang, 2008, 2011). However, detailed design of new configurations may require more complex models. For example, Figure 4 illustrates the layer design for a particular counter-flow planar fuel cell. This manifold configuration is not well represented by conventional design rules, and precise pressure drop and flow-distribution predictions may require three-dimensional CFD simulations.

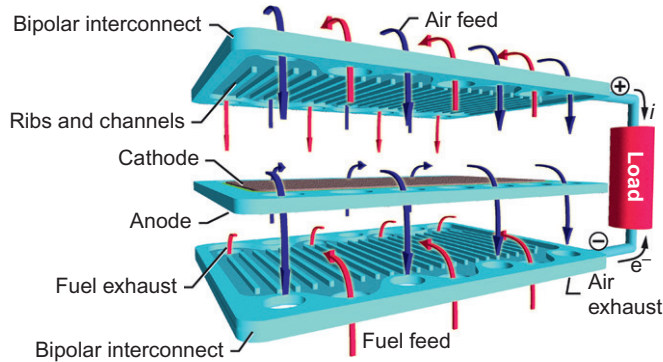


Figure 4 Exploded view of the channel-manifold layout for a planar counter-flow SOFC. This configuration is modeled after a system developed at Forschungszentrum Jülich (Gubner *et al.*, 2006).

2.4 System-level models

Broadly speaking, SOFC system models require component submodels (including the stack model) with the following attributes

- Capability to extract gross performance metrics
- Software interfaces to communicate with other submodels
- Capability to simulate off-design operating conditions
- Ability to follow transient behaviors
- Solution algorithms that are computationally efficient

With these attributes in mind, it is evident that models that are developed for the purposes of stack design could be quite different from system-level stack models. For example, Chapter 6 presents approaches for high fidelity models of MEAs and channels that involve detailed gas-phase species and energy transport in porous electrodes and elementary charge-transfer processes within the structure. Such approaches can be computationally expensive and may not be well aligned with the objectives of system-level modeling. Nevertheless, if measured performance maps are unavailable, predicting stack performance may be based upon single-channel models.

It is important to calibrate and validate models with experimental measurements. Figure 5A shows an illustrative example comparing measured polarization performance with a channel model prediction. These results are based on a 50 mm by 50 mm single-cell, planar stack operating on humidified hydrogen at different temperatures. Applying the model to other operating conditions, Figure 5B illustrates the predicted

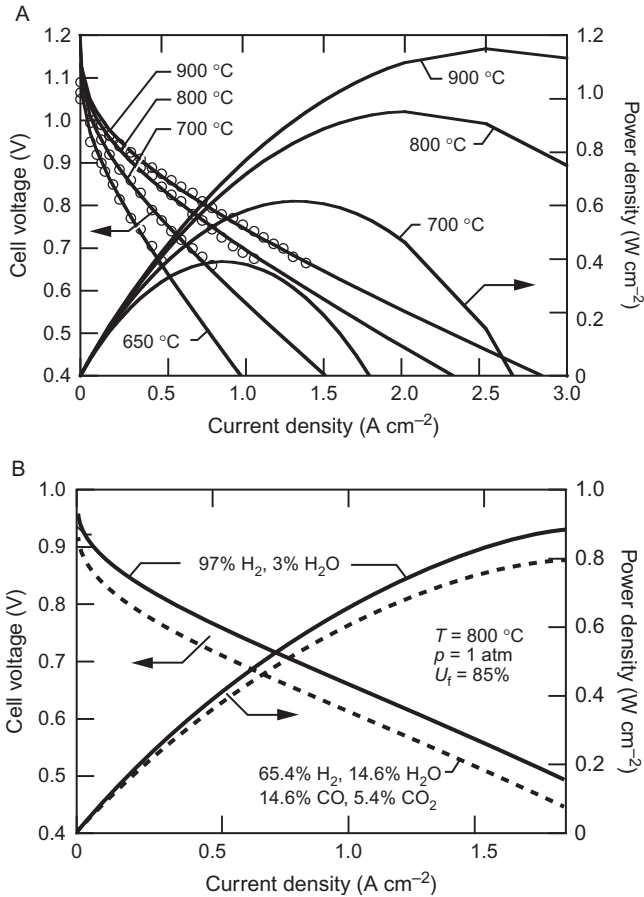


Figure 5 Illustrative polarization characteristics for a planar stack. (a) Comparison of model-predicted (lines) and experimentally measured (symbols) voltage–current performance for a planar SOFC stack operating on moist hydrogen (Ghosh, 1999). (b) Model-predicted voltage–current performance on reformat.

performance of a single channel, operating on both reformat and humidified hydrogen fuels at a constant fuel utilization of 85%. The effect of hydrogen dilution by electrochemically inactive species results in a lower Nernst potential and voltage reduction of greater than 50 mV at the same current. Power density is similarly degraded by the reformed fuel.

It is often reasonable to assume that the electrochemical performance of an entire stack may be represented by the performance of a single channel. However, if stack-level behaviors (e.g., flow distribution and pressure drop in the manifold structures) are not modeled accurately,

significant system-level errors can result. Such errors are particularly pronounced when thermal interactions between stack and system components are neglected. The following section discusses approaches for modeling system-level thermal interactions.

2.5 System thermal modeling

Typical hardware within SOFC hot-zone enclosures includes the fuel-cell stack, and balance-of-plant (BOP) components that include fuel reformer, process heat exchangers, combustors, and the piping conduits that provide interconnections among system components (see [Figure 6](#)). While separate unit processes occur within each component, external heat transport between components must be optimally managed in system-level design. Understanding component interactions and synergistically leveraging heat sinks and sources to maintain component and process temperatures are an essential aspect of the system design and optimization process.

Despite the importance of thermal interactions among components, it is not uncommon to find system-level models that largely neglect the thermal coupling. Making *de facto* assumptions that components are perfectly insulated (i.e., adiabatic) can lead to substantial errors. Such assumptions imply that all thermal communication between components is accomplished via the mass flow rates and enthalpies associated with

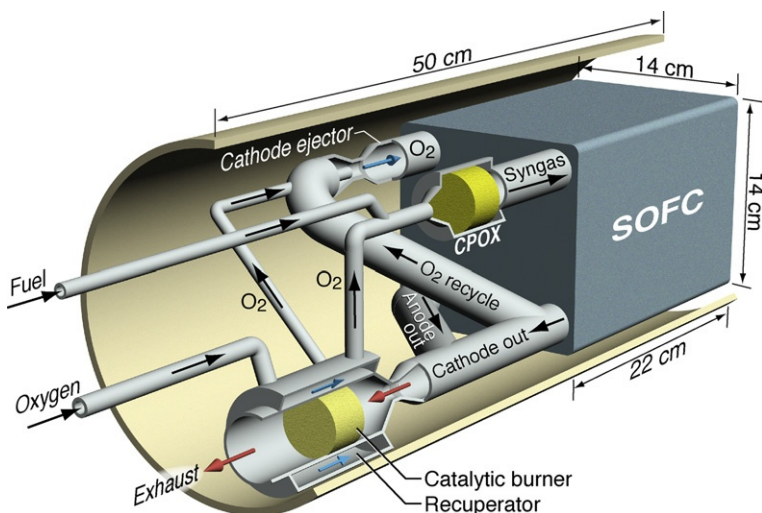


Figure 6 Possible hot-zone layout of an SOFC system for a UUV application ([Kattke and Braun, 2011a](#)).

the interconnecting gas streams. In fact, especially for small systems, at least a third of the waste heat in the system is rejected via surface heat losses to the surroundings. Additionally, thermal management is often viewed as a strategy of matching process temperatures or selection of cell-stack insulation in order to maintain cell temperature during dynamic operations, such as start-up and shutdown (Apfel *et al.*, 2006; Chen and Evans, 2005; Damm and Federov, 2006). In practice, due to thermofluidic coupling between packaged components, a change in SOFC performance alters process statepoints throughout the system and vice versa. Such effects must also be considered in system control. As discussed in previous sections, CFD software provides one means to model stack and BOP components. The following sections provide a brief overview of low-dimensional modeling techniques that may be applied to represent system thermal management, but at far less computational cost relative to full CFD.

2.5.1 Resistive model formulation

The stack is typically the largest component in SOFC systems, and its relatively high surface area and high operating temperature cause strong thermal interactions with the smaller BOP hardware (particularly in portable and mobile applications in the 1–10 kW range). Considering the dominant role of the stack in thermal management, any thermal modeling strategy must focus on enabling heat exchange between the BOP hardware and the stack. Heat rejection from the SOFC system is accomplished via two different pathways. The first pathway is heat transmission from components in the hot module to the surroundings by way of conduction and radiation through the hot-module outer surface. The second pathway is via convection of the thermal energy that accompanies the exhaust gas mass flow as it leaves the system. An overall strategy for thermal management of system heat sources and sinks depends on balancing these two pathways.

Figure 6 illustrates a possible hot-zone configuration for an SOFC power source in a small UUV (Kattke and Braun, 2011a). A lumped thermal model, based on equivalent thermal resistors, can be formulated to represent heat transport between the SOFC stack and its surroundings. Such a model, which assumes spatially uniform surface temperatures for all components and enclosure surfaces, includes conduction, convection, and radiation heat transfer mechanisms. It is often reasonable to neglect direct component-to-component interactions, compared with the interactions between a component and the surrounding enclosure walls and cavity gas. However, the validity of this assumption depends largely on system packaging. The more closely the components are packaged, the more consideration must be given to direct component–component

interactions. The net heat transfer from a component to the surroundings can be written in terms of a temperature difference divided by the equivalent thermal resistance as

$$\dot{Q}_i^{\text{cond}} = \frac{T_{w,i} - T_{\text{ins},i}}{R_{\text{ins},i}^{\text{cond}}} = \dot{Q}_i^{\text{conv}} + \dot{Q}_i^{\text{rad}}, \quad (1)$$

$$\dot{Q}_i^{\text{conv}} = \frac{T_{\text{ins},i} - T_{\text{gas}}^{\text{cavity}}}{R_i^{\text{conv}}}, \quad (2)$$

$$\dot{Q}_i^{\text{rad}} = \frac{T_{\text{ins},i} - T_{\text{HM},i}}{R_i^{\text{rad}}}, \quad (3)$$

where \dot{Q}_i^{cond} is the net heat-transfer rate from component i , $T_{w,i}$ is the lumped inner wall surface temperature of component i , $T_{\text{ins},i}$ is the insulation surface temperature of component i , $T_{\text{gas}}^{\text{cavity}}$ is the enclosure cavity gas temperature, and $T_{\text{HM},i}$ is the inner enclosure surface temperature.

Discussion of equivalent thermal resistance networks and expressions for thermal resistors can be found in any heat-transfer textbook (e.g., Bergman *et al.*, 2011). Conduction through planar walls and convection from surfaces to adjacent gases may be represented as

$$R^{\text{cond}} = \frac{L}{kA}, \quad R^{\text{conv}} = \frac{1}{hA}, \quad (4)$$

where L is the thickness through which heat is conducted, A is the area through which the heat flux is transferred, k is the material thermal conductivity, and h is a convective heat-transfer coefficient. In the so-called limit of a small body in a large enclosure, the radiation resistor is represented as

$$R^{\text{rad}} = \frac{1}{h_r A}, \quad h_r = \sigma \varepsilon (T_s + T_\infty) (T_s^2 + T_\infty^2), \quad (5)$$

where σ is the Stefan–Boltzmann constant, ε is the surface emissivity, h_r is the radiation heat-transfer coefficient, T_s is the component surface temperature (i.e., $T_{\text{ins},i}$), and T_∞ is the temperature of the surrounding enclosure (i.e., $T_{\text{gas}}^{\text{cavity}}$ or T_o).

Figure 7 illustrates a resistive network between an SOFC stack, the surrounding hot-module wall, and the external environment. Heat is transmitted by conduction from the ceramic SOFC stack surface through a layer of stack insulation material. The surface heat flux from the outer insulation material occurs through combined heat-transfer modes of convection and radiation. Radiation heat flux between the insulated stack surface and the wall of the hot module assumes grey diffuse surfaces and is accomplished with a view factor specification and linearized radiation

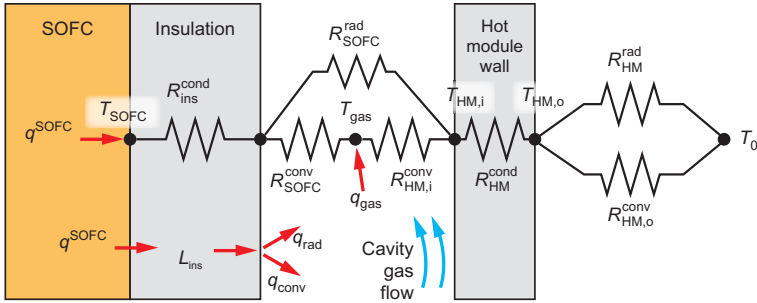


Figure 7 Equivalent thermal resistance network representing thermal interactions between an SOFC stack and its surroundings.

heat transfer coefficient. The equivalent heat transfer resistance for this network is expressed as

$$R_{tot} = R_{ins}^{cond} + \left[\left(R_{SOFC}^{rad} \right)^{-1} + \left(R_{SOFC}^{conv} + R_{HM,i}^{conv} \right)^{-1} \right]^{-1} + R_{HM}^{cond} + \left[\left(R_{HM,o}^{rad} \right)^{-1} + \left(R_{HM,o}^{conv} \right)^{-1} \right]^{-1}. \quad (6)$$

In this formulation, the hot-module wall is assumed to be sufficiently large in diameter that a plane wall representation is an appropriate simplification. Evaluating the resistances requires an estimate of the convective heat transfer from the hot-module inner wall ($T_{HM,i}$) to the enclosure gases (i.e., q_{gas}). Sensitivity of the selection of the fraction of q_{gas} to the total wall heat flux should be made, but in many cases, the overall system results are not overly sensitive to this parameter. [Braun and Kattke \(2011\)](#) have reported that a reasonable range for the q_{gas} fraction to total wall flux is 40–60% for small mobile systems (<3 kW).

The use of resistive networks is a convenient construct to represent complex thermal interactions but certainly requires several assumptions and simplifications with regard to the actual thermofluidic physics. As illustrated in [Figure 8](#), a thermal resistive network for an entire subsystem within the hot module can be developed by coupling each of the components to the inner hot-module wall temperature $T_{HM,i}$. Balance-of-plant components within the hot enclosure approximates their inner wall surface temperature by taking an average gas temperature. The stack surface temperatures are outputs from the stack thermal model. Although in this formulation components are not directly coupled to one another via radiation mechanisms, they are coupled through convection. An energy balance to the cavity gas temperature node within the enclosure is expressed as

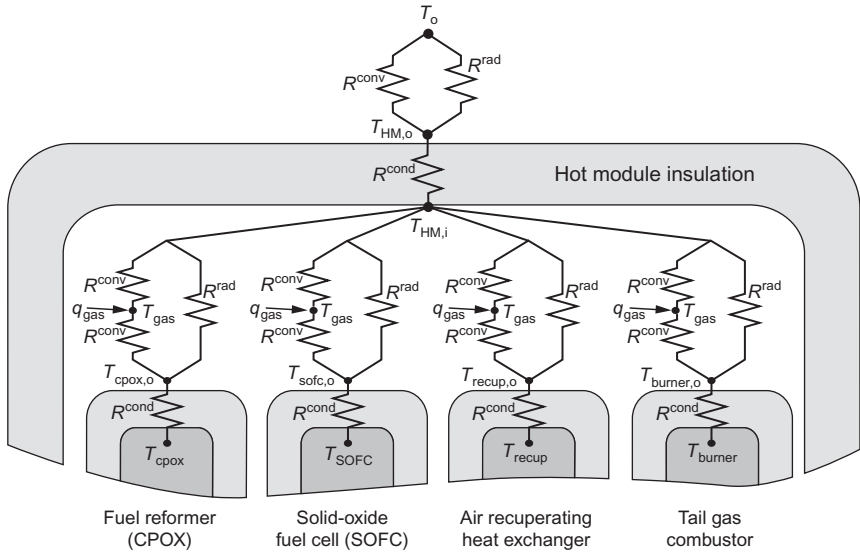


Figure 8 Thermal resistive network for system components within enclosure.

$$\dot{Q}_{\text{gas}}^{\text{cavity}} = \dot{m}_{\text{gas}}^{\text{cavity}} c_p (T_{\text{gas,in}} - T_{\text{gas}}^{\text{cavity}}), \quad (7)$$

where $\dot{m}_{\text{gas}}^{\text{cavity}}$ and $T_{\text{gas,in}}$ are the flow and temperature of the entering cavity gas, $T_{\text{gas}}^{\text{cavity}}$ is the temperature of cavity gases within the hot enclosure, and c_p is the average specific heat calculated from the inlet and cavity gas temperatures. Components are also coupled through radiation by a common interaction with the inner surface of the enclosure wall. (note that in Figure 8, the q_{gas} term is equivalent to $\dot{Q}_{\text{gas}}^{\text{cavity}}$ of Equation 7.)

Selection of component radiation view factors requires an assessment of component packing density and geometry. Employing component view factors of unity assumes a relatively large enclosure area in comparison to component areas. In the resistive thermal model approach, the radiation view factors are all assumed to have a value of 1.0 and employ a linearized radiation heat-transfer coefficient. In the case of larger system components (e.g., the stack and recuperator), where the enclosure “sees” the component, radiation exchange from larger components is expected to be overpredicted. As the components in a system are more tightly packaged, the formulation of the radiation heat-transfer resistance naturally becomes more complicated, involving radiosity, emissivity, and view factors for N surface enclosures. The source of the cavity gas flow can be either from outside cooling air or from an internal gas stream. In either situation, estimation of heat transfer from components near the inlet of

cavity gases into the enclosure will experience the greatest error, since that is where the largest departure from the assumption of perfectly mixed gas temperature occurs. Lumped surface temperatures and lack of component-to-component radiation exchange will tend to underpredict the coupling of neighboring system components. Greater fidelity in capturing component-to-component interactions requires either a more elaborate resistive network or the use of CFD.

2.5.2 System-level thermal management

When a system thermal model is integrated into a thermodynamic system process model, interactions between component heat loss (or gain) and process-gas temperatures and flow conditions are captured. The predictive nature of the resulting integrated model provides feedback to design considerations, such as component sizing and gas flow rates. In the following, the integrated thermal model is exercised on a 1.1 kW (gross) mobile SOFC system concept shown in Figure 6. The figure illustrates the general layout of the system where each unit operation is a discrete component. Although this example is for a UAV application, the essential features of the integrated thermal-system model are applicable to many other similar-sized applications.

Figure 9 illustrates a system-statepoint diagram, detailing results from an SOFC system operating with liquid dodecane ($C_{12}H_{26}$) as the fuel and pure oxygen as the oxidizer. Of particular interest is the temperature increase of $33\text{ }^\circ\text{C}$ between oxidant entering the stack module and that

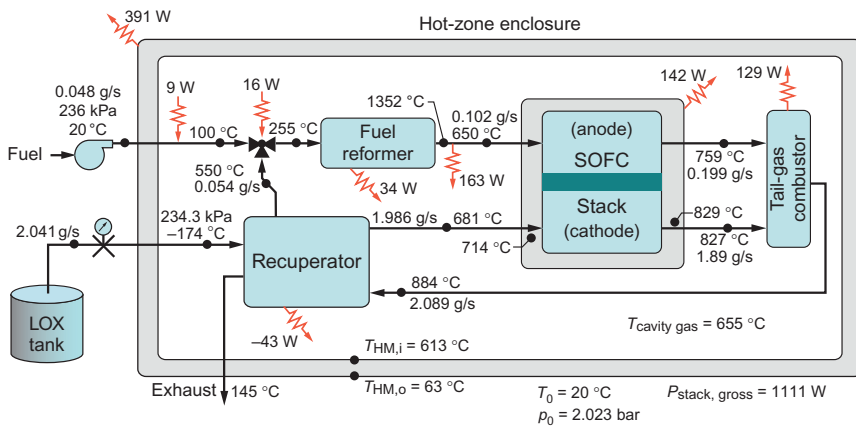


Figure 9 Thermally integrated SOFC system with quantified thermal interactions within enclosure.

entering the cathode compartment of the stack itself. At a stack operating temperature of 800 °C, a relatively cold oxidant stream at 681 °C is required to enter the oxidant inlet manifold of the stack. The solid stack remains relatively hot at the oxidant inlet, 714 °C, which presents a large temperature driving force for heat transfer to manifold cavity gases entering the stack module. Stack manifold and surface heat transfer strongly influence the cooling-air flow rate that is needed to maintain the stack operating temperature. Greater than 75% of the 142 W of heat loss from the stack outer surface is transferred via radiation to the enclosure inner wall. Because radiation is a significant heat-transfer mechanism, its inclusion in the system thermal model is very important to the fidelity of the model.

The model enables design alternatives to be explored, such as introducing a cooling gas flow within the enclosure, insulation thickness, etc. System thermal models show that cathode gas flows are typically overestimated by as much as 200% in small-scale systems when adiabatic assumptions are used (Braun and Kattke, 2011). Oxidant usage is especially important in mobile applications where the oxidant must be stored onboard (e.g., underwater applications). Further, heat transfer within gas manifolds influences temperature distribution within the stack. Because the stack-level thermal performance is sensitive to oxidant flow rate, it is important to develop thermally integrated system models.

2.6 Fuel processing considerations

Fuel processing is defined herein as the conversion of a commercially available gas or liquid fuel to a gaseous reformat that is suitable for serving the fuel-cell anode reactions without cell performance degradation. Fuel processing encompasses the removal of harmful contaminants, such as sulfur, the generation of a hydrogen-rich gas stream, and heating (or cooling) of the reformat to the prescribed inlet temperature of the fuel-cell stack. In low-temperature fuel cells, the fuel processing may also include additional measures beyond desulfurization and reforming, such as low- and high-temperature shift conversion and preferential selective oxidation.

Direct electrochemical oxidation of hydrocarbons, including methane, within SOFC anodes is difficult to accomplish in conventional SOFCs. Therefore, carbonaceous fuels are reformed to produce syngas (H_2 and CO). The extent of fuel processing depends not only on the fuel-cell type but also on the fuel type. Alcohols (e.g., methanol or ethanol) and hydrocarbons (e.g., natural gas) are usually reformed into a hydrogen-rich synthesis gas using one of several possible methods: catalytic steam

Table 1 Possible global reactions in reforming processes

Name	Reaction	ΔH_{298} (kJ mol ⁻¹)
Steam reforming	$\text{CH}_4 + \text{H}_2\text{O} \rightleftharpoons \text{CO} + 3\text{H}_2$	206.1
Water-gas shift	$\text{CO} + \text{H}_2\text{O} \rightleftharpoons \text{CO}_2 + \text{H}_2$	-41.15
Reverse Sabatier	$\text{CH}_4 + 2\text{H}_2\text{O} \rightleftharpoons \text{CO}_2 + 4\text{H}_2$	165.0
Dry reforming	$\text{CH}_4 + \text{CO}_2 \rightleftharpoons 2\text{CO} + 2\text{H}_2$	247.3
Methane cracking	$\text{CH}_4 \rightleftharpoons \text{C}(\text{s}) + 2\text{H}_2$	74.82
Boudouard	$2\text{CO} \rightleftharpoons \text{C}(\text{s}) + \text{CO}_2$	-173.3
CO reduction	$\text{CO} + \text{H}_2 \rightleftharpoons \text{C}(\text{s}) + \text{H}_2\text{O}$	-131.3

reforming (CSR), CPOX, or ATR (U.S. Department of Energy, 2004). Table 1 lists several global reactions for the reforming of methane.

The raw fuel can be converted and reformed external to the SOFC in a reactor (often a packed-bed type) or internally within the anode compartment. Most external reformer concepts for stationary applications favor CSR, because it yields the highest amount of hydrogen and results in the highest system efficiencies (Carrette *et al.*, 2001). By contrast, CPOX offers compactness, fast start-up, and rapid dynamic response, but sacrifices fuel conversion efficiency. ATR is a combination of CSR and CPOX processes. In general, these reforming technologies all share approximately the same level of complexity. The major technological difference between CSR, CPOX, or ATR processes is the mechanism for providing the thermal energy required for the endothermic reforming reactions (Larminie and Dicks, 2003).

2.6.1 Desulfurization

Sulfur-bound fuels include logistic fuels, gasoline, coal-gas, biogas, heating oils, and natural gas. Sulfur is a poison to essentially all fuel cells and must be removed from the fuel feedstock before it is admitted into the reformer and cell stack. The reforming reaction requires a catalyst (typically nickel or rhodium) with high surface area supported on a ceramic substrate (e.g., alumina). The conventional anode of the SOFC is also nickel-based, which promotes electrochemical charge transfer as well as internal reforming (IR). The nickel catalyst in both the reformer and fuel cell is poisoned by the sulfur compounds normally found in many fuels. Even the normal odorant compound level in natural gas rapidly deactivates the catalyst due to tenacious adsorption and formation of nickel sulfide (Gong *et al.*, 2007; Zha *et al.*, 2007). Thus, because fuel-bound sulfur compounds poison both the reforming catalysts and the fuel-cell electrocatalysts, they must be removed from the raw fuel feedstock. The

allowable sulfur concentration for intermediate temperature (700–850 °C) SOFCs is limited to about 0.1 ppmv (Ivers-Tiffée *et al.*, 2009; Zha *et al.*, 2007), above which substantial electrode performance degradation is realized. Current research is considering new anode materials and novel electrode structures to overcome these issues (cf. Pillai *et al.*, 2008; Yang *et al.*, 2009a). Nevertheless, until such electrode developments mature, desulfurization of the fuel gas will be required.

Several desulfurization techniques are available, including activated carbon, zinc oxide, and hydrodesulfurization (Larminie and Dicks, 2003). Both zinc oxide and hydrodesulfurization processes require operation near 400 °C. Generally speaking, desulfurization technology is well established and the choice of technique depends upon cost-effectiveness and the type of sulfur compounds present in the fuel.

2.6.2 Catalytic steam reforming

Due to wide availability of light hydrocarbon gases (i.e., natural gas) for stationary applications, this section focuses on steam reforming of natural gas. Natural gas is a fuel mixture that is methane rich but contains low levels of some higher hydrocarbons (e.g., ethane, propane, and butane) and nitrogen. Natural gas reformers for SOFC systems usually operate near atmospheric pressure and, because the cell operating temperature is sufficiently high, may be thermally integrated with the fuel-cell stack such that the necessary heat for the endothermic reforming reactions is supplied by the heat release from electrochemical oxidation of hydrogen and ohmic losses associated with current generation and flow in the cell stack. CSR is capable of operating with high fuel conversion efficiency (85–95%). As illustrated conceptually in Figure 10, at least three different reforming configurations are possible: (1) ER, (2) indirect internal reforming (IIR), and (3) direct internal reforming (DIR). Because CSR is an endothermic process, ER requires a heat source, such as a burner or hot waste gas. IR capitalizes on the heat release in the fuel oxidation process by providing a

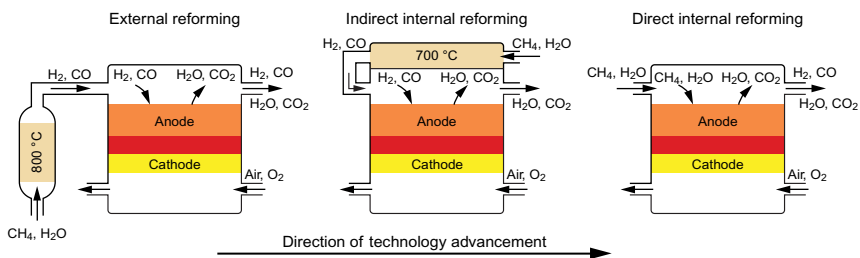


Figure 10 Fuel-Cell CSR Configurations (adapted from Hartvigsen and Khandkar, 1994).

convenient and efficient setting for energy transfer between heat source and heat sink. Such tight thermal coupling can also reduce the required cathode air flow rate, which is often used to control stack temperature.

The close coupling of CSR within the SOFC anode (i.e., DIR) offers other potential benefits, including the reduction of parasitic power and reduced cost. The heat produced by inefficiencies associated with charge-transfer chemistry and ohmic heating can be delivered directly to support endothermic reforming. However, DIR still requires some partial “pre-reforming” external to the fuel cell, reforming some of the methane and higher hydrocarbons in the primary fuel. The partial reforming is needed to eliminate carbon deposits in the fuel cell and to limit temperature gradients. If the endothermic reforming reactions proceed too rapidly near the cell inlet, the associated cooling can produce deleteriously large temperature gradients. External CSR reformers can have relatively slow dynamic response times, thus limiting the dynamic response of the entire system. Faster load response is anticipated for DIR–SOFC systems due to the close proximity of reaction processes and the reduced mass of the fuel-processing system (Meusinger *et al.*, 1998).

A significant concern during reforming operation is the formation of solid carbon through undesired side reactions known as methane decomposition (or cracking), Boudouard coking, and CO reduction, respectively, which are listed in Table 1. Carbon deposition should be avoided as it deactivates catalyst and clogs interstices within the reactor bed or porous anode microstructure. Boudouard and CO reduction reactions are both exothermic and the forward rate reduces the number of moles. Thus, low temperature and high pressure favor these reactions. Because CO is usually not present in the fuel, and hence at the reformer inlet, these carbon deposition reactions are not thermodynamically favored. Nevertheless, as methane is consumed and carbon monoxide is produced, carbon deposition reactions can become thermodynamically and kinetically possible when the gas is cooled below 750 °C (Sasaki and Teraoka, 2003). Even when conditions conducive to carbon deposition are present, the reaction kinetics may be so slow that deposits are not significant over the life of the catalyst.

The problem of determining when or where carbon formation will occur is presently limited to evaluating thermodynamic tendencies. Accurate prediction of carbon deposition can only be achieved by experiment or analysis with the appropriate kinetic rate equations. However, the rate equations are generally not known (Sasaki and Teraoka, 2003; Wagner and Froment, 1992). Consequently, the tendency for carbon formation can be estimated by evaluating the spatially varying equilibrium state within the reformer. The risk for carbon formation through side reactions is reduced by increasing the SC ratio of the fuel feedstock. However, the

minimum amount of steam necessary for carbon-free operation is difficult to establish.

Estimating the minimum SC ratio based on evaluation of thermodynamic driving forces results in excessive but “safe” SC ratios of usually 2 or 3 to 1. Wagner and Froment (1992) have used the principle of equilibrated gas to make a conservative estimate of 1.6 as the minimum SC ratio to prevent coking phenomenon. The validity of this method increases with increasing operating temperature. Others have employed phase equilibria via C–H–O ternary diagrams (e.g., Sasaki and Teraoka, 2003).

Figure 11A shows the temperature-dependent equilibrium hydrogen yield for a steam-to-methane ratio of 2:1. As temperature increases, H₂ production begins at about 150 °C, increases in a nearly linear fashion from 300 to 700 °C, and reaches a maximum hydrogen yield near 800 °C and above. Thus, Figure 11A offers some insight into the motivation for the selection of reformer operating temperature.

In addition to suppressing carbon deposits, the SC ratio also affects the equilibrium yield of hydrogen. Figure 11B shows the effect of SC ratio on the equilibrium species mole fractions at 800 °C and 1 atm. As the SC ratio is increased, the hydrogen concentration decreases. Increasing the SC ratio also negatively affects the overall system energy efficiency by (1) requiring additional primary steam generation or recycle of anode effluent for reforming, and (2) by increasing the mole fraction of water vapor in the exhaust gas, the sensible heat available in the exhaust gas for heat recovery is reduced (Rienschke *et al.*, 1998a). These considerations clearly illustrate the incentive to minimize the steam requirements for fuel processing.

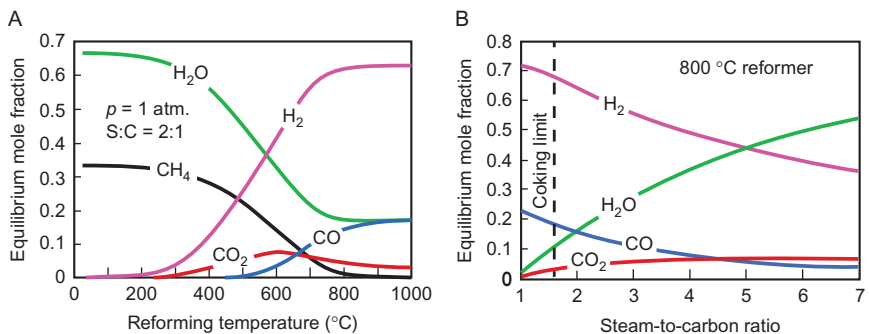


Figure 11 Equilibrium predictions for CSR. (a) Equilibrium reformate composition from CSR as a function of reactor temperature. (b) Effect of steam-to-carbon (SC) ratio on equilibrium reformate composition.

2.6.3 Catalytic partial oxidation and autothermal reforming

Hydrogen can also be liberated from methane and other hydrocarbons through partial oxidation, which may be catalyzed, noncatalyzed, or a combination of both (Carrette *et al.*, 2001). The partial-oxidation process is typically used to reform heavy hydrocarbon and oil fuels where the required heats of reaction are provided *in situ* by oxidizing a fraction of the feedstock (Larminie and Dicks, 2003). Because CPOX yields lower levels of hydrogen per mole of hydrocarbon input than CSR processes, as well as consuming a portion of the fuel heating value to supply the heat for the endothermic reforming reaction, it results in lower system efficiencies (approximately 3–10% below systems using CSR). Overall, CPOX is an exothermic process. Despite these inefficiencies, CPOX reformers are attractive for mobile power applications where the inefficiencies are acceptable in light of other advantages, such as cost, weight, and dynamic response (Braun and Kattke, 2011; Burke and Carreiro, 2006; Miller and Reitz, 2010).

ATR is a hybrid technology that combines steam reforming methods with the *in situ* oxidation feature of partial-oxidation technology. Endothermic steam reforming and exothermic CPOX are combined to produce near thermal neutrality of the overall process. The operating temperature of the ATR process (≈ 850 °C) is usually lower than that of CPOX (1100–1500 °C) and higher than that of CSR (≈ 800 °C). Unlike CSR, both CPOX and ATR processes produce a syngas stream that is diluted by nitrogen when air is used as the oxidant. Because ATR offers many of the same advantages of CPOX reforming, but with higher efficiency, developers are increasingly considering its use for mobile and residential systems.

3. ANALYSIS OF SOFC SYSTEMS

The analysis of system performance and operating behaviors contributes significantly to achieving optimal design. For example, high electrochemical fuel utilization is necessary to achieve high system electric efficiency yet may be less desirable in a CHP application where the thermal energy coproduct can be augmented by low fuel utilization operation. Despite numerous potential applications, several performance metrics are common to all systems. Relevant performance metrics include fuel utilization, component, subsystem and system efficiencies, heat loss and thermal management, and capital cost. This section provides relevant performance definitions, discusses system-wide operating characteristics, and presents an exergetic (availability) analysis of a small SOFC–CHP system. System cost and optimization are discussed in Section 4.

3.1 Performance definitions

Several different measures of efficiency are helpful in analyzing SOFC systems; these include

- Cell-stack efficiency

$$\eta_{\text{SOFC}} = \frac{P_{\text{DC}}}{(\dot{N}_{\text{fuel,in}} \text{HHV}_{\text{fuel}})_{\text{anode inlet}}}, \quad (8)$$

- Net system electrical efficiency

$$\eta_{\text{sys,e}} = \frac{P_{\text{AC,net}}}{(\dot{N}_{\text{fuel,in}} \text{HHV}_{\text{fuel}})_{\text{system inlet}}}, \quad (9)$$

- System cogeneration efficiency

$$\eta_{\text{CHP}} = \frac{P_{\text{AC,net}} + \dot{Q}_{\text{rec}}}{(\dot{N}_{\text{fuel,in}} \text{HHV}_{\text{fuel}})_{\text{system inlet}}}, \quad (10)$$

- Exergetic electric efficiency

$$\varepsilon = \frac{P_{\text{AC,net}}}{(\dot{N}_{\text{fuel,in}} A_{\text{fuel}})_{\text{system inlet}}}, \quad (11)$$

In these definitions, P_{DC} is the stack DC power developed, $P_{\text{AC,net}}$ is the net system AC power, \dot{Q}_{rec} is the rate of thermal energy recovered from the SOFC system exhaust gas, $\dot{N}_{\text{fuel,in}}$ is the molar system fuel flowrate, HHV_{fuel} is the higher heating value of the fuel, and A_{fuel} is the exergy (availability) of the fuel entering the system. The in-cell fuel utilization refers to the amount of fuel electrochemically oxidized within the anode compartment of the cell stack. For example, when the fuel cell is operated with natural gas reformat containing methane, hydrogen, and carbon monoxide, the fuel utilization is defined as

$$U_{\text{f,cell}} = \frac{\dot{N}_{\text{H}_2,\text{consumed}}}{(4\dot{N}_{\text{CH}_4} + \dot{N}_{\text{H}_2} + \dot{N}_{\text{CO}})_{\text{anode inlet}}}, \quad (12)$$

where \dot{N}_k is the species molar flow rate. The denominator of Equation (12) represents the maximum amount of hydrogen that could be supplied

with 100% conversion via the reforming and shift reactions. When AGR is used, the per-pass or cell fuel utilization is as given in Equation (12). However, the overall system fuel utilization is evaluated at the system inlet (i.e., not the cell inlet) as

$$U_{f,\text{sys}} = \frac{\dot{N}_{\text{H}_2,\text{consumed}}}{(4\dot{N}_{\text{CH}_4})_{\text{system feed}}}, \quad (13)$$

The amount of oxidant required is often expressed in terms of either oxidant utilization, U_o , or air "stoichs" on an oxygen basis, λ_{air} . Oxidant utilization is written as

$$U_o = \frac{\dot{N}_{\text{O}_2,\text{consumed}}}{\dot{N}_{\text{O}_2,\text{supplied}}} \quad (14)$$

where $\dot{N}_{\text{O}_2,\text{consumed}}$ is the molar rate of electrochemical oxygen consumption at the cathode and $\dot{N}_{\text{O}_2,\text{supplied}}$ is the molar rate of oxygen supplied to the cell. The molar rate of oxygen consumption is proportional to the rate of hydrogen oxidation at the anode (i.e., $\dot{N}_{\text{O}_2,\text{consumed}} = 1/2\dot{N}_{\text{H}_2,\text{consumed}}$). The number of air stoichs is then

$$\lambda_{\text{air}} = \frac{1}{U_o} \quad (15)$$

For methane-fueled systems, λ_{air} is given as

$$\lambda_{\text{air}} = \frac{\dot{N}_{\text{O}_2,\text{system}}}{2\dot{N}_{\text{CH}_4,\text{system}}}, \quad (16)$$

where the molar flow rates are evaluated at the system feed to the plant. The amount of air flow can then be determined from oxidant utilization and the molar proportion of oxygen and nitrogen in ambient air (i.e., 3.76 mol of N_2 for every mole of O_2 in simple dry air). Total air flow supplied to the system is usually greater than the stoichiometric requirements and is determined via energy balances that include the cell polarizations, the amount of IR, and the allowable temperature rise in the cathode air flow.

3.2 Operating characteristics

3.2.1 Internal reforming

The high operating temperature of the SOFC coupled with the catalytic activity of the nickel-based anode enables DIR within the fuel electrode without the need for ER equipment. However, complete IR is frustrated by a number of practical considerations, including unacceptably large thermal stresses and deleterious carbon deposition. As a result of such

limitations, present SOFC technology cannot accomplish 100% DIR within the fuel electrode. In the near-term, some fraction (20–50%) of the methane must be converted in an external pre-reformer.

The pre-reformer serves two primary purposes: (1) convert the higher hydrocarbons found in pipeline natural gas into H_2 and CO, perhaps slipping some CH_4 and (2) generate sufficient hydrogen at the anode inlet so that electrical energy can be generated at the leading edge of the cell, but under conditions where carbon deposition is unfavorable. In some cases, the pre-reformer serves the additional purpose of acting as a recuperative heat exchanger that raises the fuel feedstock to a prescribed cell inlet temperature.

Consider again the fuel reforming subsystem in the flowsheet of [Figure 1](#). Varying the inlet fuel composition to the SOFC anode can be accomplished by a combination of

- Adjusting the SC ratio,
- Controlling the reforming temperature,
- Controlling the extent of pre-reforming.

The first two approaches were discussed previously. In the present analysis, the extent of pre-reforming ξ is varied at near-ambient pressure, while maintaining a fixed reforming temperature and SC ratio. Further, only steam and pure methane species are considered at the inlet. Without pre-reforming ($\xi=0$), no hydrogen is produced and methane and steam are the only species entering the anode chamber. Complete pre-reforming ($\xi=1$) means that all of the methane is converted to a mixture of H_2 , CO, CO_2 , and H_2O , which enters the anode chamber. For CSR of methane with $SC=2$ and $\xi=1.0$, the fuel gas consists of about 65% hydrogen on a molar basis. [Figure 12](#) illustrates the effect of varying the amount of pre-reforming on cell heat and power generation, and efficiency. As the extent of pre-reforming (or conversion) increases, the cell power remains nearly constant, the net heat generation increases, and the cell efficiency decreases. The cell power remains nearly constant because the cell voltage (and Nernst potential) increases only slightly (< 50 mV) with increasing conversion. Over the entire range of methane conversion, the net heat generated in the cell increases by over 250%. It is interesting that the cell efficiency decreases by over 10% in response to a greater fuel energy input for the same power output. As the conversion of methane increases, the volumetric heating value of the fuel gas mixture at the anode inlet decreases. A disproportionate increase in the amount of hydrogen flow (relative to the decrease in heating value) is needed to maintain the same current. Thus, an increase in fuel energy input for the same power output is realized.

[Figure 12](#) also shows the effect on the cooling-air requirements and air temperature rise as the extent of pre-reforming is varied. The number of

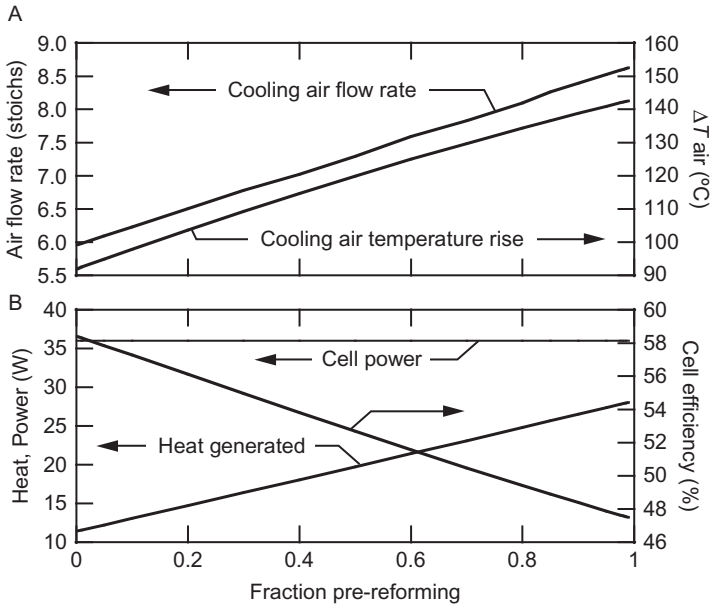


Figure 12 Influence of methane conversion in pre-reformer on SOFC heat and power generation and cooling-air indices for 800 °C cell, 700 °C inlet air, 0.5 mA cm⁻², $U_f=85\%$, and $SC=2.0$.

air stoichs required to maintain a nominal cell temperature of 800 °C increases by nearly 50% when going from 0% to 100% methane conversion. If a constant air temperature rise across the cell were maintained instead of an average cell temperature, the air stoichs λ_{air} required would increase by over 200%. DIR clearly reduces the need for excess cooling air and the associated air temperature rise.

Figure 13 illustrates the SOFC temperature and temperature-gradient profiles within a channel of a planar SOFC. Comparing Figure 13A and B reveals that while increasing the amount of pre-reforming produces higher peak temperatures, it results in a more uniform temperature-gradient distribution, contributing to reduced thermal stress.

Locating the reforming process within the anode enables the heat generation associated with the ohmic and activation polarizations to directly serve the endothermic steam reformation reactions, thereby reducing the cell-stack cooling requirements and the air blower parasitic power. IR can reduce cathode air flow requirements, and hence parasitic blower power, by greater than 50% when compared to ER. The corresponding air preheater heat-exchanger requirements can be lowered by greater than 75% (Braun *et al.*, 2006). In addition to air flow requirements, ER affects system design and performance in terms of balancing

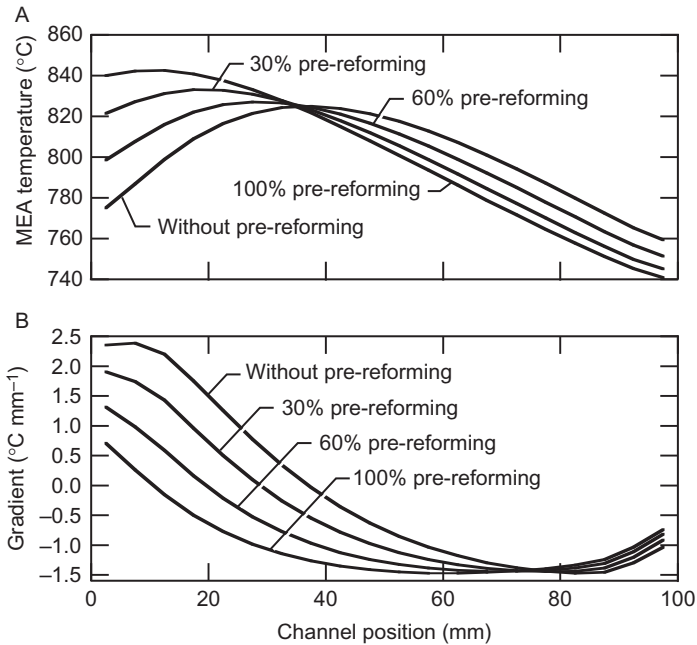


Figure 13 Influence of methane conversion on cell temperature and temperature-gradient profiles for an 800 °C cell, 700 °C inlet air, 0.5 mA cm⁻², $U_f = 85\%$, and $SC = 2.0$.

system-wide thermal requirements. For example, as the heat required to support an external reformer increases with increasing methane conversion (decreasing IR), less thermal energy is available in the fuel-cell product gases to serve the other system process needs.

IR affects system performance in several important ways:

1. Net system power and efficiency increase with IR due to reductions in parasitic power, and use of high-grade waste heat from the cell reactions for local fuel reformation (see also Section 3.3.3),
2. Net electric power increases, but less thermal energy is available for exhaust gas heat recovery,
3. Capital cost decreases due to reduced air blower and air preheater requirements,
4. Capital cost decreases due to reduction (or elimination) of ER hardware.

3.2.2 Anode gas recycle

Anode exhaust gas recycle is a system concept whereby a fraction of the depleted anode exhaust is recirculated to the fuel-cell inlet, providing water vapor to the anode feed gas to assist methane reformation and inhibit carbon deposition. The extent of AGR is defined on a molar basis as a fraction of the depleted anode exhaust gases as

$$\text{AGR} = \frac{\dot{N}_{\text{recycle}}}{\dot{N}_{\text{anode,outlet}}}. \quad (17)$$

The extent of AGR is typically chosen by balancing the need for water vapor with the thermodynamic tendency for carbon formation, especially on Ni. Increasing SC tends to negatively affect the overall system energy efficiency by requiring additional primary steam generation or recycle of anode effluent for reforming.

The primary advantage of AGR, compared to systems employing a waste-heat boiler, is the large improvement in CHP efficiency (by as much as 15%). At least two effects are responsible for the high CHP efficiency: (1) the increase in thermal energy available for heat recovery due to elimination of the waste-heat boiler and (2) a reduction in water vapor content in the exhaust gas which enables higher sensible thermal energy recovery.

At the stack level, AGR reduces in-cell (or per-pass) fuel utilization. For example, a system fuel utilization of 85% leads to an in-cell fuel utilization of about 69% when operating with an SC = 2.0. Cell-stack efficiency performance is usually enhanced by lower in-cell fuel utilization, but that effect can be negated by the dilution of H₂ and CO concentrations in the inlet anode feed stream due to the recycle stream (Yi *et al.*, 2005), particularly for systems that do not incorporate IR (Braun *et al.*, 2006).

An additional advantage of AGR can be the reduction of fuel preheating heat-transfer area by direct contact mixing of the fuel feed and the anode exhaust gas. Recirculation of fuel-cell exhaust gases can be achieved by high-temperature blowers, fans, or gas ejectors. Ejectors are usually the most cost-effective. However, disadvantages are the high compression energy required for a natural-gas-driven ejector and control of recycle throughout the operating envelope.

3.2.3 Cathode gas recycle

Cathode gas recycle is a system concept wherein cathode exhaust gases are recirculated to the fuel-cell inlet to reduce the size of the air preheater and blower components, thereby reducing the system cost. CGR also provides an opportunity to enhance system efficiency through a net reduction in the blower parasitic power requirements. The extent of cathode gas recycle is defined on a molar basis as

$$\text{CGR} = \frac{\dot{N}_{\text{recycle}}}{\dot{N}_{\text{cathode,outlet}}}. \quad (18)$$

Gas ejectors or recycle blowers are used to accomplish the cathode exhaust gas recycle. The merit of incorporating cathode recycle using

ejector devices depends on ejector efficiency and the pressure drop in the recycle loop. As with AGR, in practice the use of a gas ejector can be difficult to implement because of difficulty in controlling the amount of recycle throughout the operating envelope. Off-design operability may also require a small air preheater to ensure air temperature control at the stack inlet if recycle performance is poor. High-temperature recycle blowers are another possibility, although the service temperature requirements are severe. Systems incorporating high-temperature recycle blowers would accomplish much of the same effect as ejectors by reducing air preheater requirements, while still offering reduced overall parasitic power (Braun *et al.*, 2006).

3.2.4 Cell operating voltage

The SOFC stack is the heart of the power plant, and the selection of where to operate on its voltage–current performance characteristic is a critical consideration. Changes in cell design, operating parameters, and control strategies will produce varying system thermal-to-electric ratios (TERs), as well as impact BOP component sizing, system economics, and cell performance. The BOP is defined to be all system components except the SOFC cell stack. The present section focuses on how the selection of cell parameters influences the BOP and system-level performance characteristics for the flowsheet configuration shown in Figure 1. A 5-kW_{net} SOFC cogenerator fueled with natural gas and 80% IR serves as an example to frame the discussion. Presuming a fixed stack size (≈ 280 cells, each with a 100×100 mm planform), Figure 14 shows the sensitivity of system performance to variations in cell voltage. Figure 14A shows the impact of operating voltage on the gross cell-stack DC power, net system AC power, and air blower parasitic power. As cell voltage decreases, the gross stack power increases until it reaches a maximum of 21 kW near 0.42 V cell^{-1} . The net AC stack power output is lower than the gross power, primarily due to inverter inefficiency and the auxiliary power requirements. Net system power reaches a maximum of 13.3 kW at 0.51 V. At maximum net AC power, air blower power requirements reach 4.6 kW, which is 25% of the gross AC power (after inversion) and over 90% of the total plant parasitic power. As cell voltage decreases (cell current increases), the net AC power is reduced as blower power consumption exceeds the incremental increase in power developed by the stack. The inclusion of parasitic power requirements suggests a more practical design operating cell voltage range between 0.55 and 0.85 V. The allowable design voltage range is further reduced to 0.65–0.85 V when the potential for nickel electro-oxidation in conventional Ni-YSZ anodes is considered (Nehter, 2007; Sarantaridis *et al.*, 2008).

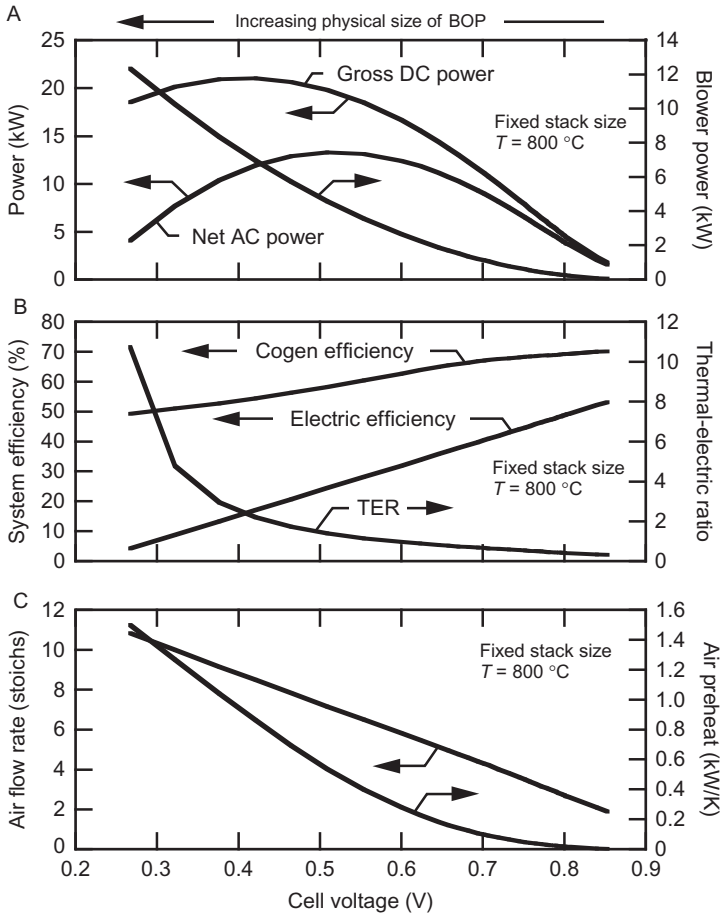


Figure 14 Influence of cell voltage on system performance parameters: (a) stack and air blower power, (b) system efficiency and system thermal to electric (TER) ratio, and (c) air flow and heat-exchanger UA requirements.

Figure 14B depicts the effect of cell voltage on system efficiencies and TER. As the cell voltage increases (power decreases), the system electric efficiency increases nearly linearly and ranges from 35% to 53% over the practical design voltage range of 0.65–0.85 V. Interestingly, the cogeneration efficiency increases slightly with increasing cell voltage, indicating that the amount of heat output nearly offsets the loss in net electric power produced at lower cell voltages. The cogeneration efficiency changes by less than 6% over the same practical voltage range. The system TER increases with decreasing voltage, ranging from $0.3 < \text{TER} < 0.8$. Many

commercial building applications require TERs nearly twice this range for domestic hot water demand and can be a factor of 10 or more greater for space heating needs, depending on geographic location and building type. Clearly high TERs are only available at low voltages (i.e., low efficiencies) which are usually impractical.

Figure 14C shows the influence of cell voltage on the cooling-air requirements to maintain a nominal cell temperature of 800 °C. The air flow, expressed in terms of stoichs, varies as $2 \leq \lambda_{\text{air}} \leq 5$ in the acceptable voltage range. Higher air flow translates into higher parasitic power and larger air preheater heat-exchanger areas.³ Air preheater conductance (i.e., UA) depends on both gas stream temperature differences and flow rates. The air preheater UA requirements are a highly nonlinear function of cell voltage; and a 44-fold increase in UA is required for a sevenfold increase in net AC power produced over the same voltage range.

3.2.5 Heat loss

Heat loss in high-temperature fuel-cell systems can be significant, ranging from 3% to 20% of the fuel energy input. The amount of heat loss depends on the module size, geometry and packaging, insulation material and thickness, and the component operating temperatures. Heat loss in small-scale (<10 kW) SOFC systems is particularly important. For example, the thermal energy loss from a 2-kW planar SOFC stack module consisting of a cylindrical vessel containing the cell stack, air and fuel preheaters, and combustor can be as high as 9-10% of the fuel energy input (Kattke and Braun, 2011b). This result reveals that heat loss is significant, and while highly variable due to size and design dependencies, it must be considered in systems modeling and analysis efforts. Approaches to account for heat loss in small SOFC systems are explored further by Kattke and Braun (2011a,b) and Kattke *et al.* (2011).

3.3 Exergy analysis

Although energetic performance assessments are valuable and necessary, an exergetic (or availability) analysis is more revealing and quantitatively insightful toward understanding the location and magnitude of process inefficiencies within a system. Exergy is a thermodynamic property that can be evaluated quantitatively in terms of other, perhaps more familiar, thermodynamic properties (Moran, 1989; Moran and Shapiro, 2008;

³Heat exchangers are often characterized quantitatively in terms of UA, which is a measure of the thermal resistance between the hot and cold flow streams (Bergman *et al.*, 2011; Kays and London, 1998; Shah and Sekulić, 2003). Although UA is best understood as a single parameter, it is the product of an overall heat-transfer coefficient U ($\text{W m}^{-2} \text{K}^{-1}$) and an effective heat-transfer area A (m^2).

Szargut, 2005; Szargut *et al.*, 1988). The change in available energy associated with the performance of a particular component can be evaluated in terms of the exergy of the inlet and outlet flow streams. Because exergy may not be a familiar concept, the following section discusses the basic elements. The equations for estimating the thermodynamic property exergy are first introduced, and an exergy analysis of an SOFC power system is then carried out to quantify component exergy destructions and efficiencies.

3.3.1 Evaluation of exergy

The exergy of a system (e.g., a flowing fluid or a fixed mass) is a thermodynamic property that represents the maximum theoretical work that can be obtained when the system comes into equilibrium with its environment. The discussion here is specific to flowing fluid streams (either ideal gas mixtures or pure component fluids) within an energy conversion system. An important reason to evaluate the exergies of process-flow streams is to assist the evaluation of second-law efficiencies of components. As discussed in the foregoing paragraphs, the exergy A is a state variable (J mol^{-1}). The exergy A_k of a species k (Jmol_k^{-1}) may be considered as the sum of thermomechanical and chemical components as

$$A_k = A_k^{\text{tm}} + A_k^{\text{ch}}. \quad (19)$$

The first term on the right-hand side represents the maximum “work” that can be obtained by bringing species k from the process-flow state to the environmental state by thermomechanical processes alone (e.g., expansion through a turbine). That is, thermomechanical (or physical) exergy is a measure of a fluid stream’s departure from thermal (i.e., temperature), mechanical (i.e., pressure), velocity, and elevation equilibrium with a stationary reference environment. The second term in Equation (19) represents the maximum work possible by converting the substance into environmental species (mainly carbon dioxide and water) at the environmental conditions. In other words, chemical exergy represents the free-energy change in converting process species k into environmental species at the environmental conditions. This term represents the maximum work that can be obtained via chemical reactions and mixing of nonreacting species.

Specification of a reference environment is particularly important as the exergy of a substance cannot be quantified until an environmental reference state, defined by its temperature, pressure, and chemical composition, is chosen. Several standard environments are available to choose from including that given by Szargut *et al.* (1988) and Moran and Shapiro (2008). Property evaluation methods for the exergy of a substance are

readily found from the literature (see Moran, 1989; Moran and Shapiro, 2008; Szargut, 2005) and are only briefly highlighted here.

The thermomechanical exergy of a flowing fluid per unit mass is written as

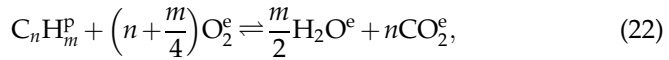
$$a^{\text{tm}} = [h(T, p) - h(T_0, p_0)] - T_0 [s(T, p) - s(T_0, p_0)] + \frac{\mathbf{V}^2}{2} + gz, \quad (20)$$

where h is the mass enthalpy, s the mass entropy, \mathbf{V}^2 and gz are the stream kinetic and potential exergies, respectively, and a is in units of kJ kg^{-1} . When evaluating the exergy of an ideal gas mixture, it is convenient to use molar specific properties, where exergy is the sum of the partial exergies of the constituents,

$$A_{\text{mix}}^{\text{tm}} = \sum_k X_k [(H_k(T) - H_k(T_0)) - T_0 [S_k(T, p) - S_k(T_0, p_0)]]. \quad (21)$$

In this expression, the kinetic and potential exergy contributions have been neglected and X_k is the mole fraction of the k th component in the mixture. H_k is the molar enthalpy, which is a function of temperature alone. The molar entropy S_k is a function of temperature and pressure. In evaluating Equation (21), the chemical composition is assumed to be frozen at the process-flow conditions. Chemical reaction and composition change are captured in the chemical component and are added to the thermomechanical component to get the total exergy of a stream as given in Equation (19).

The first step in evaluating the chemical exergy is to write a reversible reaction for each species k in the process flow. The objective is to react the process-flow species with an environmental species, creating as products only species that are in the environment. For instance, the reaction of a hydrocarbon fuel may be written as



where the superscripts “p” and “e” refer to the species being in the process-flow state and environmental state, respectively. The chemical contribution to the exergy of a process-gas species k is

$$A_k^{\text{ch}} = -\Delta G_k^{\circ} - RT_0 \ln \left(\prod_{j=1}^K (X_j^{\text{e}})^{v_{j,k}} \right), \quad (23)$$

where ΔG_k° is the change in standard state Gibbs free energy for the reaction of species k , $v_{j,k}$ is the stoichiometric coefficient of species j , R is the universal gas constant, and X_j^{e} is the species mole fractions in the environment. For example, the chemical exergy for methane is

$$A_{\text{CH}_4}^{\text{ch}} = -\Delta G_{\text{CH}_4}^{\circ} - RT_0 \ln \left[\frac{\left(X_{\text{CO}_2}^e \right) \left(X_{\text{H}_2\text{O}}^e \right)^2}{\left(X_{\text{O}_2}^e \right)^2} \right]. \quad (24)$$

The logarithmic term typically only contributes a few percent to the magnitude of the chemical exergy (Moran and Shapiro, 2008), and the chemical exergy of a hydrocarbon fuel is often found to be within 3–9% of its lower heating value (Wark, 1998).

Process gases of interest in SOFC applications include hydrocarbons, oxygenated fuels (e.g., alcohols), syngas (H_2 and CO), as well as environmental gases including H_2O , CO_2 , O_2 , and N_2 . Solid fuel feedstocks, such as biomass and coal, supplied to energy systems involving SOFCs are also receiving increasing interest. Generalized methods for evaluating chemical exergy of gases and fuels are given in Moran and Shapiro (2008) and Wark (1998).

On a molar basis, the total exergy can be expressed as

$$A^{\text{tot}} = \sum_{k=1}^K X_k A_k = \sum_{k=1}^K X_k (A_k^{\text{tm}} + A_k^{\text{ch}}). \quad (25)$$

To evaluate the potential power (Watts) associated with a particular process flow, the molar flow rate (mol s^{-1}) is multiplied by the exergy of the process flow. Thus, the *exergy rate* (Watts) of a flow is determined as

$$\dot{A} = \dot{N} A^{\text{tot}}. \quad (26)$$

3.3.2 Exergetic balances and efficiencies

In an exergy analysis, exergy balances are made on each component within the system with the objective of quantifying the exergy destruction rate. The exergy destroyed represents the loss of work potential as a consequence of process irreversibilities within the device. Assuming that heat Q crosses control surfaces, work W is done by (or on) the component, and mass flows across possibly multiple inlets and exits, a generalized exergy rate balance for a component can be formulated as

$$\frac{dA_{\text{cv}}}{dt} = \sum_j \left(1 - \frac{T_o}{T_j} \right) \dot{Q}_j - \left(\dot{W}_{\text{cv}} - p_o \frac{dV_{\text{cv}}}{dt} \right) + \sum_i \dot{m}_i a_i^{\text{tot}} - \sum_e \dot{m}_e a_e^{\text{tot}} - \dot{A}_D \quad (27)$$

where A_{cv} is the total exergy of the control volume, \dot{Q}_j is rate of the heat transfer across surface j at temperature T_j , \dot{W}_{cv} is the net rate of work transfer, \dot{M} is the rate of mass flow at the inlet or exit of the system, and \dot{A}_D is the rate of exergy destruction. The first term on the right hand side of

Equation (27) represents the exergy transfer accompanying the net heat transfer into the control volume. The second term is the net work transfer within the control volume and is inclusive of moving boundary work. The exergy accompanying mass transfer into and out of the control volume is given by the third and fourth terms in Equation (27), respectively.

Second law efficiency definitions are varied and depend upon the purpose of the device or system. A typical definition places the useful product exergy in the numerator and all exergetic inputs in the denominator according to

$$\varepsilon = \frac{\sum \dot{A}_{\text{out}}^{\text{useful}}}{\sum \dot{A}_{\text{in}}} \quad (28)$$

3.3.3 Exergy analysis of a SOFC–CHP system

For the purposes of demonstrating an exergy analysis, consider a 1.3 kW methane-fueled SOFC system with heat recovery that is operating at near-atmospheric pressure with 100% ER (Figure 15). In this configuration, a waste-heat boiler provides superheated steam at 5 bar with a SC ratio of 2:1 for the external reformer. The boiler is located immediately downstream of the fuel reformer to ensure that a sufficient pinch temperature is achieved. Air is preheated to 729 °C before delivery to the SOFC cathode compartment. The SOFC module operates at a nominal temperature of 800 °C and 0.705 V cell⁻¹, producing 2.0 kW of DC power at a cell-stack efficiency of 40.5% (44.2% LHV). The air blower consumes about 0.53 kW to supply the cooling air at 315 mbar, and 1.3 kW net AC power is generated at an overall system HHV efficiency of 34.0% (37.8% LHV). A large fraction of the thermal energy in the combusted product gas is required to support endothermic fuel processing reactions in the reformer. After the air preheater, the product gas (112 °C) is further cooled to about 51 °C in the hot water heating system, providing 0.95 kW of low-grade (60 °C) hot water. The system is capable of an overall cogeneration efficiency of 58.5% (64.9% LHV).

Figure 16 shows the energy and exergy flows for an externally reforming natural-gas fueled system. Approximately 3.9 kW of energy in the form of natural gas enters the system and is transformed through mass addition and thermochemical energy conversions to nearly 5.6 kW at the anode inlet. The energy supplied to the fuel-processing system from the balance of plant is approximately 1.7 kW. About 5 kW of the 5.6 kW of energy delivered to the anode compartment is in the form of chemical energy and the remainder in thermal energy. Thus, the process of fuel reformation using fuel-cell product gases serves to increase the magnitude of the chemical energy (and exergy) of the fuel gas stream delivered to the SOFC stack.

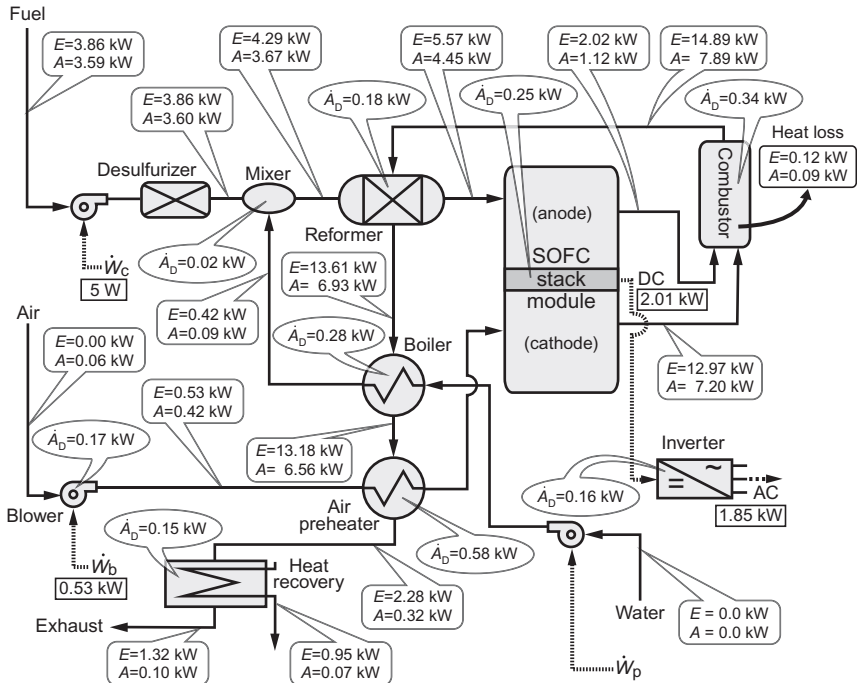


Figure 16 Process flowsheet for a 1.2-kW methane-fueled SOFC CHP system with external reforming. The rounded rectangular callouts show energy E and exergy A for the process flows, the oval callouts show loss of exergy within the devices, and the sharp rectangular callouts show electrical or thermal power.

combined with methane and thermal energy, boosts the exergetic fuel content fed to the stack and thereby reduced the overall natural gas input to the system. Braun *et al.* have shown this to be the primary reason that methane-fueled SOFC systems are of higher electric efficiency than those fueled with pure hydrogen, even when the hydrogen is “free” and no IR is used (Braun *et al.*, 2006). In contrast, a hydrogen-fueled SOFC system degrades the high-grade thermal energy content of the exhaust stream to produce more low-grade hot water, thereby increasing the CHP efficiency but reducing the electric efficiency (Braun *et al.*, 2006).

The exergy rates shown in Figure 16 indicate that the primary system irreversibilities are located in the air preheater (26%), catalytic combustor (19%), boiler (12%), and SOFC stack (11%). The exergy rate of the system effluent is less than 3% of the fuel input. Additionally, the exergy content of the delivered hot water system is only 0.07 kW, compared to the 0.95 kW of thermal energy valuation associated with 60 °C water. Of the 0.43 kW

of exergy consumed (i.e., lost) in the combustor, approximately 78% is due to irreversibilities of the combustion process (chemical reaction, thermal energy exchange between reactants and products, and mixing) and 22% as a result of heat transfer to the surroundings. The exergy analysis suggests that system improvements should be concentrated on reducing the air preheater duty and improving catalytic combustion by reducing the mixing loss.

4. TECHNOECONOMIC MODELING AND OPTIMIZATION OF SOFC SYSTEMS

The importance of technoeconomic analyses is the ability to quantify benefits of CHP operation and optimize a system design by judiciously taking into account the competing objectives of capital and operating cost minimization subject to both system design and application constraints. Fuel-cell system performance characteristics are largely driven by cell-stack design parameters such as cell voltage, fuel utilization, operating temperature, and cathode gas temperature rise. As previously observed (see Figure 14), depending on where the fuel-cell stack is operated on its voltage–current characteristic, different proportions of electric and thermal output will be derived from the fuel-cell system. Selection of design parameters may maximize either power density or electric efficiency. Further, the design operating point strongly influences the capital costs of the major system hardware components, such as the SOFC stack, air blower and preheater, and heat recovery equipment. The operating costs are primarily associated with fuel consumption (or efficiency). Quantitatively understanding and predicting the cost–benefit trade-offs is the objective of technoeconomic modeling.

4.1 Life cycle costing

Minimizing LCC is usually the basis for system optimization. The LCC is defined to mean the net present worth of the sum of all capital and operating costs throughout the life of the system. For an electric-power-generation application, the LCC may be expressed in terms of the leveled cost of electricity (COE). In stationary SOFC applications, the COE and LCC may be based on either electric-only or CHP systems where the waste heat provides value. Cost models incorporate the forecasts for manufacturing costs of the SOFC and BOP components. The models consider capital and maintenance costs, utility energy prices (grid electricity and natural gas), interest and energy inflation rates, and system efficiency.

In an electric-only application, the COE (e.g., \$/kWh)⁴ can be expressed as

$$\text{COE}_{\text{eo}} = \underbrace{\frac{\text{CRF} \times C_{\text{eo}}^{\text{sys}}}{A_{\text{plant}} \times \text{CF}_e}}_{\text{System capital cost}} + \underbrace{\sum_j \text{MC}_j}_{\text{Maintenance}} + \underbrace{\frac{F_c}{\eta_e^{\text{sys}}}}_{\text{Fuel cost}}. \quad (29)$$

The first term in this expression is associated with the capital costs, the second term with maintenance costs, and the third term with fuel costs. The capital recovery factor (CRF) is defined to mean the ratio of a constant annuity and the present value of receiving that annuity for a specified period of time. The installed capital cost for an electric-only system is expressed as $C_{\text{eo}}^{\text{sys}}$ (e.g., \$/kW). The system electric capacity factor CF_e is defined to mean the ratio of the electricity produced and the electricity that would have been produced if the plant operated 100% of the time at its rated capacity. The expected annual plant availability is A_{plant} . The levelized annual maintenance cost of component j is MC_j (e.g., \$/kWh). The unit fuel cost is F_c (e.g., \$/kJ). The system electric efficiency is η_e^{sys} (HHV basis). The levelized annual maintenance cost for each component j may be evaluated by forecasting the present worth of all replacement costs over the life of the plant as

$$\text{MC}_j = \frac{\text{CRF} \times C_j \left[\frac{(1+i_{\text{infl}})^{n_1}}{(1+i)^{n_1}} + \frac{(1+i_{\text{infl}})^{n_2}}{(1+i)^{n_2}} + \dots \right]}{\text{CF}_e + A_{\text{plant}}}, \quad (30)$$

where the numerator represents the present worth of annual payments for the replacement cost of component j replaced in years n_1, n_2, \dots , utilizing an equipment-cost inflation rate i_{infl} and an interest rate i . The component cost is represented as C_j . Levelized maintenance costs are estimated by amortizing each of the expected service requirements over the life of the system. For example, mature SOFC stacks are often assumed to have an operational life of 5 years (40,000 h), with some salvage value as a percentage of the original investment. These considerations translate into replacing the entire fuel-cell stack two times during a 15 year plant life. In similar fashion, other replacement costs, such as catalysts in the reformer and combustor, may be replaced every 5 years (40,000 h) and the sorbent bed in a desulfurizer is typically replaced annually.

In a CHP system, the net COE must be offset by the thermal energy that is recovered and used for either process, space, or hot water heating,

⁴ Monetary cost is represented as \$, meaning any appropriate currency (e.g., dollars).

$$\text{COE}_{\text{CHP}} = \underbrace{\frac{\text{CRF} \times C_{\text{CHP}}^{\text{sys}}}{\text{CF}_e}}_{\text{System capital cost}} + \underbrace{\sum_j \text{MC}_j}_{\text{maintenance}} + \underbrace{\frac{F_c}{\eta_e^{\text{sys}}} \left[1 - \text{CF}_h \frac{\eta_{\text{CHP}} - \eta_e^{\text{sys}}}{\eta_{\text{htg}}} \right]}_{\text{Fuel cost - Thermal energy credit}}, \quad (31)$$

where $C_{\text{CHP}}^{\text{sys}}$ is the installed cost for fuel cell and cogeneration systems (e.g., \$/kW). The factor η_{htg} represents the heating efficiency of the system that is being displaced by the recovered thermal energy from the SOFC. The capacity factors CF_e and CF_h represent the electric-generating and heating functions, respectively. The net thermal energy conversion efficiency is equivalent to $\eta_{\text{CHP}} - \eta_e^{\text{sys}}$, where η_{CHP} is the system cogeneration efficiency. Transmission and distribution costs do not factor into the COE for on-site power generation.

The LCC of an SOFC system can alternatively be evaluated by adapting the P_1 - P_2 method developed by [Duffie and Beckman \(2007\)](#) for the case of grid-connected fuel-cell power systems that may not supply 100% of the electricity and/or thermal energy requirements of an application. In the P_1 - P_2 method, the LCC is considered to be the sum of two terms ($\text{LCC} = P_1F + P_2C$) that are proportional to the first year operating cost F and to the system installed capital costs C . The LCC of an SOFC power system is then expressed as

$$\text{LCC}_j^{\text{SOFC}} = P_1 \left(F_j^{\text{SOFC}} + F_{\text{ngas}}^{\text{utility}} \right) + P_2 C_j^{\text{sys}} \dot{W}_{\text{net}}^{\text{sys}} + P_3 F_{\text{elec}}^{\text{utility}} (1 - \text{CF}_e \times A_{\text{plant}}), \quad (32)$$

where the subscript j refers to either an electric-only or CHP type system, F_j^{SOFC} is the annual fuel cost to operate the SOFC system, $F_{\text{ngas}}^{\text{utility}}$ is the annual natural gas fuel cost of the utility charges to serve the thermal energy demand in the application, $\dot{W}_{\text{net}}^{\text{sys}}$ is the rated power capacity of the SOFC system, $F_{\text{elec}}^{\text{utility}}(1 - \text{CF}_e \times A_{\text{plant}})$ is the net grid electricity cost to deliver power to the application demand that is not met by the fuel-cell system. The constants P_1 and P_3 are present-worth factors that depend primarily on the number of years that the equipment is expected to operate, the inflation rate for expenses related to operation (typically the rate at which the cost of the fuel or electricity inflates), and the market discount rate. The constant of proportionality P_2 depends on many economic parameters, including the down payment on the first costs (capital and installation), the interest and market discount rates, depreciation, salvage values, etc.

Detailed capital cost data for SOFC systems is given by [Braun \(2010\)](#), [Gerdes et al. \(2009\)](#), [Arsalis et al. \(2009\)](#), and [Thijssen \(2007\)](#), and can be used to generate cost functions (cf. [Braun, 2010](#)) that are employed to estimate the first costs, such as in Equation (32). LCC

objective functions can be developed to optimize the hardware configuration in a system or to optimally select design parameters within a given system configuration. Optimization of the system configuration for SOFCs has been explored parametrically (Braun, 2010; Riensche *et al.*, 1998b) and more recently using mixed-integer linear and nonlinear programming (Autissier *et al.*, 2007; Palazzi *et al.*, 2007; Pruitt *et al.*, 2011).

An objective function is formulated from minimization of the system LCC subject to constraints such as mass and energy conservation, property relations, and performance characteristics of all hardware within the system. Performance characteristics involve heat-exchanger effectiveness or approach temperatures, fuel-cell voltage–current characteristic, blower and pump pressure rise–flow characteristics, extent of conversion in the reformer, etc. The optimization problem is highly nonlinear and usually involves several independent variables to optimize on as discussed in the subsequent section.

4.2 Optimal parameter selection

Important SOFC stack operating parameters include nominal cell voltage, fuel utilization, cell temperature, and allowable cathode air temperature rise. Optimal selection of each of these parameters involves observing constraints, such as minimum air flow requirements (i.e., $\lambda_{\text{air}} > 1$), and recognizing that these parameters are not independent of one another. Additional considerations involve the practical realities of how operating conditions affect the relationships between cell life and durability. The following example considers the performance of a small SOFC micro-CHP system that is based on the process-flowsheet given in Figure 1.

4.2.1 Optimal cell voltage and fuel utilization

Figure 17B shows how variations in cell voltage and fuel utilization affect the electric efficiency and the number of cells in the SOFC stack that are required to meet a given net AC power load. As the nominal single-cell voltage increases, the system efficiency increases and cell power density decreases. Over the range of cell voltage explored, the system efficiency increases from 31% to 51% (HHV) and the number of cells in the SOFC stack increases by over 300%. Figure 17A shows the implications of these trends in terms of normalized LCCs for both electric-only and CHP systems. Life cycle fuel costs are reduced with increasing cell voltage by an amount greater than incremental increases in system first costs associated with the fuel-cell stack. This trend persists until the increase in the capital cost, due to the increasing

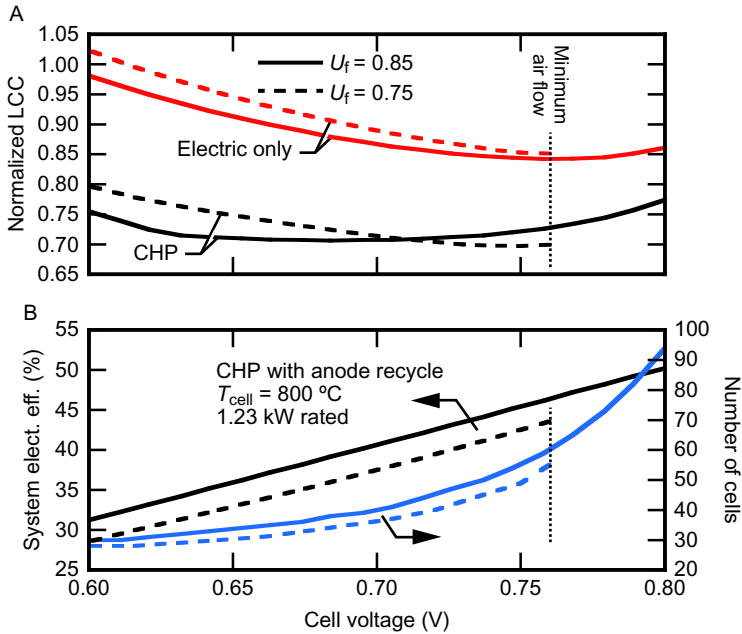


Figure 17 The effect of cell voltage on normalized LCC, system efficiency, and stack size.

number of cells in the stack to produce the required amount of power (i.e., cell power density), offsets the efficiency gains. For fuel utilization of 85%, optimum cell voltages are observed at 0.685 and 0.76 V for CHP and electric-only systems, respectively. Figure 17A also shows that the CHP configuration realizes 1–12% lower LCC, depending on operating voltage. When fuel utilization decreases from 85% to 75%, LCCs increase throughout the voltage range for the electric-only system. The reason for this trend is that lowering fuel utilization not only increases cell power density (reducing capital cost) but also reduces system efficiency (increasing operating costs). In the case of CHP configurations, the reduction of electric efficiency due to lower fuel utilization can be offset by the increase in waste-heat recovery, such that fuel utilization of 75% ultimately yields the lowest LCC at a cell voltage of 0.75 V. Simultaneous exploration of the cell voltage and fuel utilization parameter space indicates that a global optimum is likely at 0.75 V and 75% fuel utilization. For systems intended for electric-only applications, the minimum LCC favors higher cell voltage and higher fuel

utilization, while a balance is struck between voltage and fuel utilization for CHP systems.

4.2.2 Optimal cell temperature and air temperature rise

Figure 18A shows that increasing cell operating temperature reduces cell polarization, resulting in improved efficiency. The cost model incorporates the change in SOFC stack and air recuperator material requirements as operating temperature is varied from its nominal value of 800 °C and the cell model responds to changes in cell resistance due to changes in operating temperature. Figure 18B illustrates that as the cell operating temperature increases from 700 to 850 °C, the normalized LCC decreases by as much as 10%. This figure also shows the sensitivity of LCC to changes in cell voltage and temperature. When the operating voltage increases from its baseline value of 0.7 to 0.75 V cell⁻¹ at a given temperature, the LCC decreases. This characteristic is largely due to the benefits of reduced fuel costs from increased operating efficiency. Further, higher capital cost at higher operating temperature can be mitigated, or even

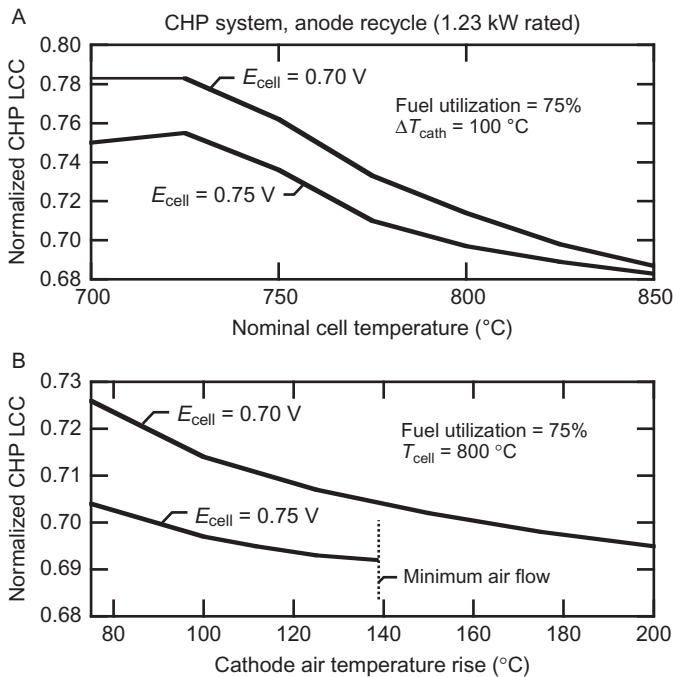


Figure 18 The effect of cell temperature and air temperature rise on normalized SOFC-CHP LCC.

reduced, as second order effects, such as reduced air flow and therefore reduced air preheater duty and cost, compensate for higher SOFC capital costs. However, Figure 18A reveals that the benefits of selecting a higher design cell voltage diminish with increasing operating temperature as gains in cell efficiency and airflow reduction are nonlinear and are ultimately bounded by the minimum system air flow requirements.

The variation of LCCs is also analyzed for changes in design air temperature rise across the cathode. This analysis assumes that it is possible to achieve acceptable levels of thermally induced internal cell stresses due to the increased cell temperature gradient via stack and cell design strategy. The plots in Figure 18B are generated by maintaining the nominal cell operating temperature at 800 °C, but varying the allowable cathode air temperature rise across the cell. An increase in cell temperature rise from 75 to 200 °C reduces the LCC metric by 4% for a nominal 0.7 V cell⁻¹ condition and by less than 2% for a 0.75 V cell⁻¹ operating point. It is further observed that the use of 100% IR and operation at higher cell voltages leads to LCC optima constrained by minimum airflow requirements. Figure 18 shows that, in general, the opportunity to reduce the LCC of the system design is greater for increases in cell operating temperature than for increases in the allowable air temperature rise.

The results of this study suggest that the optima are driven toward solutions that maximize cell temperature and air temperature rise, minimize cell voltage and fuel utilization, and approach or reside at the constraint of minimum air flow (Braun, 2010). Within a given material temperature range, maximizing cell temperature increases system efficiency and cell power density, and decreases SOFC capital cost. Increasing the cathode air temperature rise reduces BOP capital cost and increases system efficiency through reductions in air blower parasitic power, but in increments that are smaller than those gained by increasing cell temperature. Reduction of cell voltage, and hence system efficiency, can be overcome by increases in cell temperature and allowable air temperature rise. These observations indicate that the optimal values of LCC are achieved by maximizing system efficiency and minimizing the number of cells in the stack (the highest capital cost component) until parameter constraints in cell temperature, $\Delta T_{\text{cathode}}$ or λ_{air} are reached. Although the analysis presented herein is for a small SOFC-CHP system, similar conclusions also apply to larger SOFC CHP systems.

Practical considerations in selection of SOFC design parameters are heavily influenced by cell life and durability. Increasing cell temperatures and reducing design voltages (increasing current density) generally reduce cell lifetime (Linderth and Mogensen, 2000). Further, a 40,000-h SOFC stack with an average voltage degradation rate of 0.5%/1000 h will decay on the order of 160 mV cell⁻¹ from beginning-of-life to end-of-life. Thus,

end-of-life current densities must be higher to satisfy the same power demand at beginning-of-life. The systems-level perspective must account for the increased reactant flows at end-of-life and this may ultimately provide little leeway in the selection of cell voltage. Nevertheless, for the purposes of this analysis, it is insightful to quantify the benefits without such restrictions by assuming that cell voltage parameter exploration is essentially one of median cell voltage design conditions (i.e., middle-of-life performance).

5. PROCESS CONTROL

The SOFC stack requires careful balancing of fuel and air for operation, with the specific flow rates, composition, and temperature all affecting its ability to meet desired power loads efficiently and without damaging or degrading components. Such operation requires a control system to regulate the SOFC and BOP components to achieve the desired performance. Although simple regulatory loops can be used, efficiency, response speed, and safety can be significantly enhanced by using a high-performance control system that is designed using knowledge of the complete system dynamics. By analogy, it is instructive to consider the evolution of internal-combustion engines. Early engines made little use of feedback control, but current engine technology implements highly sophisticated control systems to regulate fuel and air inputs, spark and valve timing, and exhaust gas recirculation. Control systems play a central role in achieving engine performance with high efficiency and low emissions.

The control of an SOFC system has several objectives:

- Follow the load demand (i.e., provide desired electrical power).
- Maximize efficiency (i.e., maximize the ratio of produced power and chemical potential of the fuel).
- Respect constraints on input and output variables (i.e., assure that the SOFC and BOP are not damaged).

These objectives can be categorized as being related to performance (e.g., load following and efficiency) or safety and operation (e.g., limiting temperature and fuel utilization, voltage regulation). While the performance objectives relate to achieving a desired output, the safety and operational objectives relate to maintaining inputs and outputs within desired bounds. Examples of control systems that tackle one or more of the objectives can be found in the literature; for representative samples, see [Hasikos *et al.* \(2009\)](#), [Huo *et al.* \(2008\)](#), [Jurado \(2006\)](#), [Pukrushpan *et al.* \(2004\)](#), [Yang *et al.* \(2009b,c\)](#). The remainder of this chapter discusses how SOFC and BOP dynamics affect the relative difficulty of achieving these

objectives. The discussion also highlights the advantages of a particular high-performance control strategy—model-predictive control (MPC).

5.1 Physical constraints

There are numerous variables (often interrelated) that must be controlled to avoid damage within the SOFC or BOP components. One of the most important constraints in SOFC systems is maintaining operating temperature and limiting temperature gradients. Exceeding temperature limits leads to the degradation of critical components such as sintering of catalysts and electrode layers. The durability and chemical stability of metals and seals are adversely affected by high temperatures. Typical SOFCs operate at temperatures around 800 °C, but temperatures exceeding 1000 °C are likely to cause damage. The temperature of conventional metal-based heat exchangers should not exceed about 850 °C (Khandkar *et al.*, 2000; Lundberg, 1989; Veyo, 1996). High-temperature gradients can cause component damage via thermomechanical stresses that cause cracks or delamination of critical interfaces. Introduction of low-temperature gases with high local reforming rates is one mechanism that can cause high-temperature gradients. Although there is no clear consensus on the maximum allowable temperature gradients, in-plane gradients below 1 °C mm⁻¹ are considered to be acceptable (Stolten *et al.*, 2000).

Other important constraints are the inlet fuel composition, operating voltage, and fuel utilization. Fuel mixtures with high hydrocarbon content can lead to deleterious carbon deposits within the anode structure, possibly causing irreversible damage to the cell. Even small concentrations of olefins (e.g., ethylene) leaving a reformer can cause carbon deposits in the SOFC. Nickel-based anodes can be oxidized thermally by exposure to high-temperature air or by electro-oxidation caused by operating the cell below a certain low voltage (usually around 0.6 V). The large volume change associated with NiO formation eventually causes major cell damage, often leading to complete failure. Low operating SOFC voltage can also be harmful to power-electronics components.

5.2 Inputs and outputs

A control system makes use of sensor measurements (e.g., temperatures or chemical composition) to command actuation of input variables (e.g., cell voltage or fuel flow rate). One of the first tasks in controller design is to decide which variables to use as *controlled inputs* and which variables to use as *measured outputs*. In some cases, the choice of which variables to consider as inputs may not be clear *a priori*. As a

simple example, consider a resistor. This “system” has two variables of interest, the voltage across the resistor and the current through the resistor. Neither of these variables is clearly “the” input; one could consider the voltage to be the input and the current the output, or vice versa. The choice depends upon which variable is more convenient to externally specify. Other system variables affect behavior but are not inputs or outputs. For example, the resistance of the resistor is considered to be a *parameter*. In addition to controlled inputs and measured outputs, the controller must consider *disturbance inputs* and *unmeasured outputs*. Disturbance inputs are signals or boundary conditions that affect the system dynamics but are not directly controllable. Unmeasured outputs are variables of interest that cannot be measured but may be inferred from other measurements (Goodwin *et al.*, 2001).

Table 2 lists the signals that may be important to control an SOFC system. Particular choices of inputs and outputs are made that will be used in the examples that follow.

5.3 Effect of dynamics

The dynamic response between manipulated inputs and measured outputs can play an important role in determining how well the control objectives can be met. Some general observations about control systems

Table 2 Inputs and outputs for an SOFC

<i>Controlled inputs</i>	<i>Disturbance inputs</i>
Voltage, E_{cell}	Cell load I_{cell}
Inlet fuel flowrate, $m_{f,i}$	Inlet fuel temperature, $T_{f,i}$
Inlet air flowrate, $m_{a,i}$	Inlet air temperature, $T_{a,i}$
Fuel steam-to-carbon ratio, s/c	Heat Loss Q
<i>Measured outputs</i>	<i>Unmeasured outputs</i>
Current, i_{cell}	Cell temperature gradient, ∇T
Outlet fuel temp., $T_{f,o}$	
Outlet air temp., $T_{a,o}$	
Cell temp., T_{cell}	
Fuel utilization, U_f	
<i>Parameters</i>	
Cell geometry	
Cell material properties	
V - I characteristic	
Reforming reaction rate	
Flow configuration	

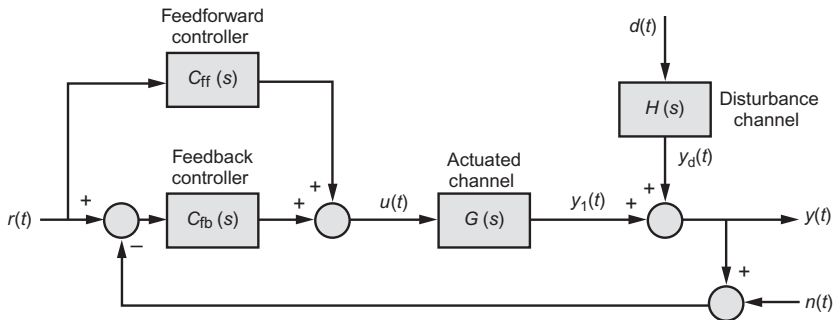


Figure 19 A simple control system with feedback and feedforward elements.

are useful in understanding the effect of dynamics. Although a more formal analysis is possible using systems theory, an illustrative set of operating guidelines can be established by considering a simple feedback control configuration as illustrated in Figure 19. In this configuration, the control objective is for the system output $y(t)$ to follow the reference command signal $r(t)$. It is also possible for the control objective to include desired trajectories for internal unmeasured signals, but for simplicity, only the measured case is included in this example. The controller is made up of computational blocks. The feedforward controller takes as its input only the reference signal. The feedback controller takes as its input the difference (error) between the desired reference and the measured output. The signals from these two controllers are summed into the actuator command $u(t)$, which is applied to the system. Complicating the ability of the control system to follow the desired reference is the possibility of a disturbance signal $d(t)$ and measurement noise $n(t)$. The behavior of the disturbance signal is modeled by a separate system $H(s)$, whose output is summed with the output of the actuated system, resulting in the net system output $y(t)$.

Each of the blocks in Figure 19 represents a differential equation that describes the relationship between the signals entering and leaving the block. The differential equation is defined by the *transfer function*, which is a rational function of the differential operator (for convenience denoted by $s := \frac{d}{dt}$). For example, the differential equation

$$\frac{d}{dt}y(t) + y(t) = \frac{d}{dt}u(t) + 2u(t) \tag{33}$$

can be rewritten using operator notation as

$$(s + 1)y(t) = (s + 2)u(t). \tag{34}$$

Formally dividing both sides by $(s + 1)$, Equation (34) can be rewritten as

$$y(t) = G(s)u(t), \tag{35}$$

where $G(s) = (s + 2)/(s + 1)$. This notation is understood to indicate that the relationship between $y(t)$ and $u(t)$ is given by the differential equation defined by $G(s)$, as in Equation (35). In this illustration, all of the differential equations are assumed to be linear. However, even though the SOFC dynamics are nonlinear, at a specific operating point, small amplitude variations of the signals will be well represented by linear equations, and the performance limitations that occur in this case will still provide valid insights into the general case.

Writing the differential equations in terms of $G(s)$ is especially useful for considering coupled systems, because the differential equation relating any pair of signals can be found by solving the set of algebraic equations defined by the input–output relationships (Equation (35)) and the summing junctions. The following transfer functions can be derived that define how the signals $r(t)$, $d(t)$, and $n(t)$ affect $y(t)$,

$$T_{yr}(s) = \frac{[G_{fb}(s) + C_{ff}(s)]G(s)}{1 + G_{fb}(s)G(s)}, \quad (36)$$

$$T_{yn}(s) = \frac{-C_{fb}(s)G(s)}{1 + C_{fb}(s)G(s)}, \quad (37)$$

$$T_{yd}(s) = \frac{H(s)}{1 + C_{fb}(s)G(s)}. \quad (38)$$

The subscripts denote the output and input variables, for example, $T_{yr}(s)$ defines the differential equation relating output $y(t)$ to input $r(t)$.

In addition to defining the differential relationships between variables, the transfer function can also be used to find the *frequency response* (i.e., how the system responds at steady state when the input is a sinusoid of a particular frequency). Specifically, given the transfer function relationship $y(t) = G(s)u(t)$, if $u(t) = \sin(\omega_0 t)$, and the system is asymptotically stable, then $y(t)$ will approach the function $|G(j\omega_0)|\sin(\omega_0 t + \angle G(j\omega_0))$, where $G(j\omega_0)$ is $G(s)$ evaluated at $s = j\omega_0$ ($j = \sqrt{-1}$). Using this fact and the form of the transfer functions (Equations (36)–(38)), important implications about the form of the control can be obtained.

5.3.1 Disturbance rejection

Consider the objectives for disturbance rejection. Suppose the disturbance is a sinusoid with frequency ω (or, alternatively, the disturbance is an arbitrary signal whose Fourier transform has significant energy at frequency ω). Attenuating the effect of this disturbance on the output requires that $T_{yd}(j\omega) \approx 0$. By observing the form of $T_{yd}(s)$, this shows the competition inherent between the disturbance channel and the actuated channel. Any frequency where $H(j\omega)$ is large requires that the product

$G(j\omega)C_{fb}(j\omega)$ to be large (and in fact, even larger) in order to achieve disturbance attenuation. In cases when the disturbance channel has a lower gain at ω than the actuator channel ($|H(j\omega)| < |G(j\omega)|$), achieving this inequality can be straightforward. However, when the reverse is true ($|H(j\omega)| > |G(j\omega)|$), the feedback control block must have high gain at $j\omega$. Such a high gain has several other implications, including the imposition of large amplitude variations in the actuator command $u(t)$ during operation, and high sensitivity to variations in the actual dynamic behavior of the actuated channel at high frequency. In fact, the use of high-gain control can be prevented by physical or operational limits to the magnitude of $u(t)$, as well as considerations of controller robustness to uncertainty in $G(j\omega)$.

SOFC controllers must consider the regulation of the current output in the face of load variations. As illustrated in Figure 20, when current is considered as an output, there are three main variables that can be actuated to control the system: fuel flow rate, voltage (in reality, voltage itself is controlled by power electronics), and air flow rate. (Not shown are fuel composition and fuel and air temperature. Fuel consumption is usually held constant while the gas temperatures have a small effect on current for small temperature variations.) The relative limitations in these actuators are also illustrated in both amplitude and frequency. The first block along each channel is a nonlinear function that shows how the commanded signal is limited in amplitude either by physical limits or desired operating range. Both fuel flow and air flow are limited to be between zero and a physical upper bound (i.e., the capability of a pump or blower), while voltage is restricted to a small range by both hardware

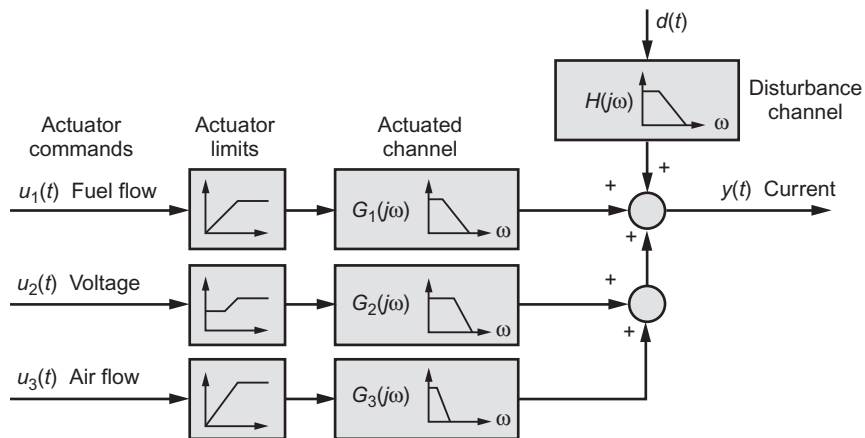


Figure 20 Illustration of cell dynamics with current as output.

limitations and to avoid damage to the stack. The second block along each channel illustrates the frequency response, with a bandwidth that is inversely proportional to the dominant time constant. The voltage channel has a large bandwidth with a dominant time constant on the order of milliseconds. The fuel flow rate has a smaller bandwidth with a dominant time constant on the order of seconds. The air flow rate has an even smaller bandwidth since the air flow primarily affects the current through a change in operating temperature and thus a dominant time constant that can be on the order of hundreds of seconds.

The discussion above indicates that disturbance-rejection control will require using multiple channels, depending upon the bandwidth and amplitude of the disturbance. Fast, high bandwidth, disturbances can be rejected using the voltage channel. However, because of practical actuator limits, high bandwidth disturbances are restricted to small amplitudes. For larger disturbances, the fuel flow channel can be used, but the bandwidth of the disturbance must match the bandwidth of the fuel flow rate channel. Specifically, large disturbances with bandwidth greater than 0.1–1 Hz will not be able to be rejected.

5.3.2 Reference following

A controlled system achieves good reference following when the output $y(t)$ closely matches the reference signal $r(t)$. An analysis similar to that for disturbance rejection can be done in this case. By definition, good reference following at frequency ω requires $T_{yr}(j\omega) \approx 1$. Thus, good reference following can be achieved when $r(t)$ is a sinusoid of frequency ω (or when $r(t)$ is a general signal with significant energy at ω), if $C_{fb}(j\omega)G(j\omega)$ is large, or if not, when $C_{ff}(j\omega) \approx 1/G(j\omega)$. There are advantages and disadvantages to each approach

- If $C_{fb}(j\omega)$ is large, then we need large actuator amplitude authority, just as in the disturbance-rejection case. In addition, because of the form of T_{yn} , good reference following will also mean that measurement noise at this frequency will be passed through to the output.
- By making $C_{ff}(j\omega) \approx 1/G(j\omega)$, we may still need a large actuator authority if $G(j\omega)$ is small, but generally the size of $C_{ff}(j\omega)$ for good tracking is less than required for $C_{fb}(j\omega)$. Also, increasing $C_{ff}(s)$ does not amplify the noise signal. However, it may be difficult to ensure that $C_{ff}(j\omega)$ is close to $1/G(j\omega)$ if $G(j\omega)$ is uncertain, or if $G(s)$ is not invertible.

Feedforward control can improve reference following in the frequencies for which $G(j\omega)$ is well known and invertible. Reference following is still subject to the same kinds of bandwidth restrictions as for disturbance rejection. Thus, good reference following cannot be achieved unless an actuated channel is available with good actuator authority at the reference

frequency. For SOFC systems, this would mean that while low amplitude current variations can be followed at millisecond time scales, large changes in the reference trajectory should be limited to the order of seconds.

5.4 Model-predictive control

In the previous discussion, the control was described in terms of an unspecified dynamical system with transfer function $C(s)$. This section considers controller implementation. However, rather than designing a particular linear system, an on-line optimization-based method called MPC is used (Morari *et al.*, 1999; Qin and Badgwell, 2003). MPC can result in a nonlinear controller, however, in the vicinity of a particular operating point, the controller behavior will be essentially linear, and the insight gained from the previous section will remain valid.

MPC makes decisions about system actuator commands based on optimization of an objective function that includes a simulation of the system behavior in the specification of required constraints. Initially developed for chemical processes with long time constants, MPC has become more feasible for faster processes because computational and algorithmic resources have improved. Today, methods are available that enable some forms of MPC to be implemented at a sample rate of over 1 kHz (Wang and Boyd, 2010).

The key advantages of MPC compared to other control implementations (such as Proportional-Integral-Derivative, or PID control) include

- Multiple-input/multiple-output (MIMO) systems can be handled,
- Hard constraints on the inputs and outputs can be enforced,
- Information from system models can be directly incorporated within the controller.

The MPC implementation is accomplished in two distinct steps: (1) estimate the current system state from observations of past inputs $u(t)$ and outputs $y(t)$ and (2) establish future actuation trajectories $u(t)$ to take the system from a current state through a desired output trajectory. Figure 21 is an illustration of data flow for MPC. Each of the light-gray blocks is part of the MPC system, implemented in a computer or embedded processor. These blocks operate at each time sample, taking in new measurements from the system and determining a new command input. The Plant Model block contains a reduced model of the system under control (in this case, represented as a state-space dynamical system). This model allows simulations to be performed over short time windows using input sequences $u(t)$ and initial state $x(t)$ chosen by the Control and State Estimation blocks.

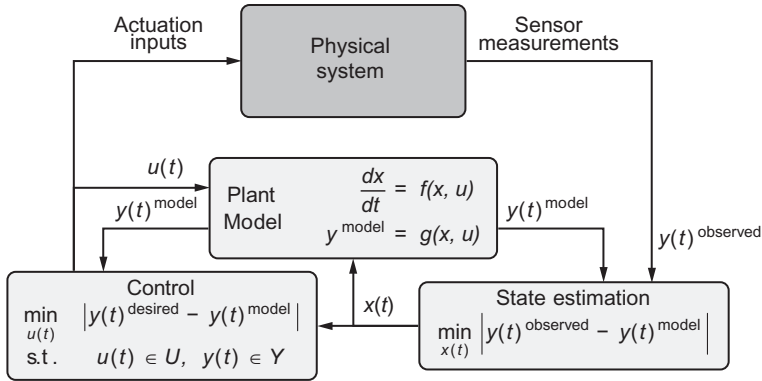


Figure 21 The data flow of model-predictive control.

The State Estimation block determines the internal system state at the current sample time. This is done via optimization: using the actual input sequence $u(t)$ that was applied up through the current time, the system state $x(t)$ at the current time (which is the final time of the simulation) is adjusted until the model output $y^{\text{model}}(t)$ best matches the observed system output $y^{\text{observed}}(t)$, with the fit measured by an appropriate objective function. In order to give this optimization process a precise mathematical description, the measurement sampling process needs to be accounted for. To do this, the following definitions are made:

- Measurements are made every \hat{t} seconds, called the sample time.
- The number of samples since $t=0$ is designated as k . The signal $x(t)$ at the k th sample is designated as $x(k\hat{t})$.
- Because the controller is also running in discrete time, the input $u(t)$ is assumed to be constant between sample points. Thus, at sample time $k\hat{t}$, the controller chooses a value u_k , and the input to the system over the next sample time is set at that value

$$u(t) = u_k, \quad k\hat{t} \leq t < (k+1)\hat{t} \tag{39}$$

- The only part of the plant model simulation that is needed are the values of the state at the sample times. Thus, in computational terms, the simulation can be abstracted as a function call that updates the state at sample time k to the state at sample time $k+1$. So if the solution to $\frac{dx}{dt} = f[x(t), u(t)]$ for $k\hat{t} \leq t \leq (k+1)\hat{t}$ has initial and final values given by $x(k\hat{t})$ and $x(k+1)\hat{t}$, an implicit functional relationship follows as

$$x((k+1)\hat{t}) = F(x(k\hat{t}), u_k), \tag{40}$$

recalling that u is constant and equal to u_k over the sample period.

Denote k_i to be the initial sample time and k_c to be the current sample time. For state estimation, it is necessary to guess a sequence of vectors x_{k_i} through x_{k_c} that represent the values of the state trajectory at the sample times (i.e., $x(k_i \hat{t})$ through $x(k_c \hat{t})$). What are the requirements for a good guess? Because the states should be expected to explain the observed output,

$$y(k\hat{t})^{\text{observed}} \approx g(x_k, u_k). \tag{41}$$

Note that u_k is the past input, and thus a known sequence. In addition, it should be expected that the states respect the system dynamics so that

$$x_{k+1} \approx F(x_k, u_k). \tag{42}$$

Finally, if any information is available about the initial state (e.g., the system starts at rest, or at a known operating point, etc.), it is expected that

$$x_{k_i} \approx \bar{x}, \tag{43}$$

where \bar{x} is the best guess for the initial state. The true state trajectory is estimated by finding a sequence x_{k_i} through x_{k_c} that best achieves a weighted combination of the three requirements above. To measure errors, an appropriate metric is chosen. The most common metric is the weighted Euclidean norm: given length n vector x , this norm is defined as

$$\|x\|_Q = \sqrt{x'Q^{-1}x}, \tag{44}$$

where x' is the transpose of x . The optimization problem solved by the estimator is then represented as

$$\begin{aligned} \min_{x_{k_i}, \dots, x_{k_c}} & \|x_{k_i} - \bar{x}\|_P^2 + \sum_{k=k_i}^{k_c} \left\| y(k\hat{t})^{\text{observed}} - g(x_k, u_k) \right\|_R^2 \\ & + \sum_{k=k_i}^{k_c} \|x_{k+1} - F(x_k, u_k)\|_Q^2 \end{aligned} \tag{45}$$

The weights P , Q , and R are chosen to reflect the relative uncertainty for the initial condition, measurement accuracy, and model accuracy, respectively. Once the optimal trajectory is found, the value of x_{k_c} is chosen as the estimate of $x(t)$ at the current time. While it appears that the number of optimization variables grows as k_c becomes larger, efficient recursive implementation using extended Kalman filter is possible, which provides an approximate solution with bounded computational cost (Simon, 2006).

Once the current system state is available, the Control block (Figure 21) can use the Plant Model to determine the next action to take. Again, an optimization problem is solved, but in this case, the optimization looks

toward the future, rather than toward the past. The optimization takes place over a window from the current time k_c to K steps into the future, where K is chosen by the controller designer. The optimization variables are the state trajectory x_{k_c+1} through x_{k_c+K} (note that x_{k_c} is known) and the future input sequence u_{k_c+1} through u_{k_c+K} . These variables must be chosen such that they respect the system dynamics so that the constraint

$$x_{k+1} = F(x_k, u_k) \tag{46}$$

is satisfied at each sample time. A key requirement of the controller is that it should drive a specified subset of the system outputs along desired trajectories (i.e., reference tracking). Let $g_1(x, u)$ represent the state output mapping for these signals. Then given a desired trajectory at the sample times, y_k^{desired} , the state trajectory and input should satisfy

$$y_k^{\text{desired}} \approx g_1(x_k, u_k). \tag{47}$$

In general, it is desirable to use as little actuator effort as possible so that

$$u_k \approx 0, \text{ or } \delta u_k \approx 0, \tag{48}$$

where $\delta u_k = u_k - u_k$. Finally, if an objective is sought for the value of the state at the end of the optimization window, say \bar{x} , then it is desired that

$$x_{k_c+K} \approx \bar{x}. \tag{49}$$

The control input and state trajectory are then calculated that best achieve these requirements. Since this is done via optimization, it is relatively straightforward to impose constraints on the input and output variables. These constraints can take various forms, but a very useful type of constraint is upper and lower bounds. Thus, the constraints

$$L_u \leq u_k \leq U_u \tag{50}$$

and

$$L_y \leq g_2(x_k, u_k) \leq U_y \tag{51}$$

should be satisfied at each sample time, where L_u , U_u , L_y , and U_y are (vector) values chosen by the control designer. The inequalities are enforced element by element, and $g_2(x, u)$ is the state output mapping for the output variables for which constraints are to be applied.

The final optimization problem has the form

$$\begin{aligned} \min_{u_{k_c+1, \dots, u_{k_c+K}}, x_{k_c+1, \dots, x_{k_c+K}}} & \quad \left\| x_{k_c+K} - \bar{x} \right\|_p^2 + \sum_{k=k_c}^{k_c+K} \left\| y_k^{\text{desired}} - g_1(x_k, u_k) \right\|_R^2 + \sum_{k=k_c}^{k_c+K} \left\| \delta u_k \right\|_Q^2 \\ \text{subject to} & \quad x_{k+1} = F(x_k, u_k) \quad k_c \leq k \leq k_c + K, \\ & \quad L_u \leq u_k \leq U_u \quad k_c \leq k \leq k_c + K, \\ & \quad L_y \leq g_2(x_k, u_k) \leq U_y \quad k_c + 1 \leq k \leq k_c + K. \end{aligned} \tag{52}$$

Again, the weights P , R , and Q are chosen to balance the specific requirements concerning tracking versus control effort. Once the solution is found, the value of u_{k_c+1} is applied as the input to the system under control for the next sampling period.

The need to maintain signal constraints during operation, combined with importance of unmeasured variables such as internal stack temperature or fuel utilization, indicates the need for advanced control strategies. Because of these important operational limits, as well as the strong interaction between input variables, MPC is a natural choice for control implementation. MPC provides a means to incorporate quantitative physical understanding into real-time process-control decisions. The SOFC stack is a complex nonlinear system, with a widely disparate range of characteristic time scales. Moreover, there are multiple actuation possibilities and a variety of sensors. It is a challenging task to design and implement a control strategy that achieves optimal performance through the coordination of multiple sensors and actuators.

One potential challenge for the implementation of MPC is the computational cost of the model simulation $x_{k+1} = F(x_k, u_k)$. Detailed physical models may be available that have been used in the design stage and tuned to accurately represent system behavior. However, unless the function call represented by $F(x_k, u_k)$ can be calculated in a fraction of the sampling time, this model cannot be directly used in MPC. One might attempt to build a simpler model by hand, but when choosing which physical effects to be included, it is often difficult to balance simplicity and fidelity. As an alternative, numerical methods can be used to find a reduced-order approximation to the high-order model. This is possible because although a large number of states may be necessary to represent the full spatial behavior of the fuel-cell system, the essential dynamics between the system inputs and the important outputs usually can be well represented using a much lower order system. Efficient and flexible methods for model reduction can be based on a data-based analysis often termed System Identification (Ljung, 1999; Van Overschee and De Moor, 1996). Such a method is illustrated in Figure 22. By applying a perturbation sequence with a wide frequency bandwidth, the model output will contain a fairly complete representation of the essential dynamics between inputs and outputs. Optimization or linear algebra based methods can be easily applied to find a linear approximation of the dynamics. By repeating these experiments at different operating points and appropriately interpolating between them, a nonlinear system model valid over a wide operating range can be obtained. A detailed discussion of this process as applied to an SOFC stack model can be found in Sanandaji *et al.* (2011).

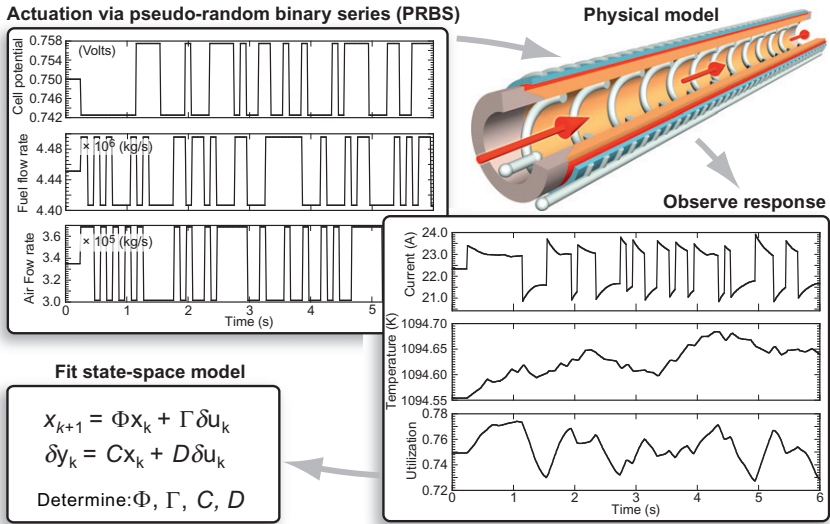


Figure 22 Decreasing model complexity via model reduction. By exercising a high-order model with perturbation sequences and observing the response, a low-order linear approximation can be obtained.

The results of the controller design developed by Sanandaji *et al.* (Colclasure *et al.*, 2011; Sanandaji *et al.*, 2011) serve as an illustration of the MPC strategy. The controller is validated using a simulated system based on a high-order model of the SOFC. The controller, however, uses a low-order model in order to reduce the computational cost in both the state estimation and control processes. The results are shown in Figure 23. The left-hand side shows the input variables that are manipulated by the controller: cell voltage, fuel flow rate, and air flow rate. The fuel composition is fixed in this simulation. On the right-hand side, the measured outputs are shown: cell current, fuel utilization, cell temperature, and air exhaust temperature. A desired cell current trajectory is shown in dark blue, while constraints to be enforced on the input and output variables are indicated by horizontal blue lines. The controller uses a look-ahead window of 2 s. Note that the controller is able to achieve large swings in current over a time period of 40 s. As reflected in the discussions of Sections 5.3.1 and 5.3.2, the controller is able to achieve this by coordinated control of the cell voltage and fuel flow. The controller allows the cell voltage to decrease because the dynamic response is fast and good tracking can be achieved. However, because of prescribed limits

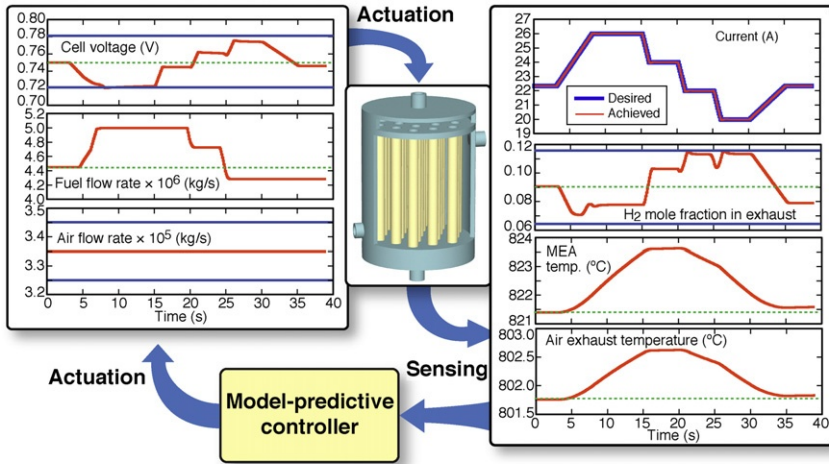


Figure 23 Results of an MPC simulation to control an SOFC through a current demand profile (upper right figure). The left-hand panels illustrate model-predicted actuation profiles and the right-hand panels show simulated sensor responses.

on the voltage, the fuel flow is also increased, which can track the larger variations, although at a longer time scale. These variables are also coordinated in order to meet the limits on fuel utilization. Because the air flow has only limited effect on the current, the controller correctly leaves this input fixed, as the temperature outputs do not change appreciably over the short time period of the experiment.

6. SUMMARY AND CONCLUSIONS

In addition to the fuel cell itself, fuel-cell system performance depends on several essential balance of plant components (e.g., fuel reformers, heat exchangers, air blowers, catalytic combustors, etc.). Understanding, optimizing, and controlling system performance are greatly assisted by models that predict the interactions of the components. Models that represent fundamental physical and chemistry, as well as geometric complexity, can be developed for the individual components. However, such models are usually too costly for application in overall system studies. These models are certainly too costly for incorporation into real-time process-control algorithms. Thus, there is a great need to develop and apply reduced-order models. At the system level, it is important to design for

thermal integration, seeking beneficial uses for heat that might otherwise be wasted. Such design considerations are assisted by thermodynamic analyses that incorporate the thermodynamic concepts of exergy (availability). Optimal system design must also consider trade-offs between the efficiency of converting fuels to electricity and the capital and operating costs. Most fuel-cell systems must deliver electrical output that follows load-demand transients. System design must be influenced by how control algorithms that meet the load demands, while also respecting constraints on input and output variables. MPC provides the means to incorporate physical knowledge into real-time control decisions, meeting load demands, respecting constraints, and optimizing performance.

REFERENCES

- Achenbach, E., *J. Power Sources* **57**, 105–109 (1995).
- Aguiar, P., Adjiman, C. S. and Brandon, N. P., *J. Power Sources* **147**, 136–147 (2005).
- Apfel, H., Rzepka, M. and Stimming, U., *J. Power Sources* **154**, 370–378 (2006).
- Arsalis, A., von Spakovsky, M. R. and Calise, F., *J. Fuel Cell Sci. Technol.* **6**, 011015 (2009).
- Autissier, N., Palazzi, F., Marechal, F., van Herle, J. and Favrat, D., *J. Fuel Cell Sci. Technol.* **4**, 123–129 (2007).
- Bergman, T. L., Lavine, A. S., Incropera, F. P. and Dewitt, D. P., *Fundamentals of Heat and Mass Transfer*, 7th ed., John Wiley and Sons, Hoboken, NJ (2011).
- Braun, R. J., *ASME J. Fuel Cell Sci. Technol.* **7**, 031018 (2010).
- Braun, R. J. and Kattke, K. J., *J. Electrochem. Soc.* **158**, B1260–B1269 (2011).
- Braun, R. J., Klein, S. A. and Reindl, D. T., *J. Power Sources* **158**, 1290–1305 (2006).
- Braun, R. J., Gummalla, M. and Yamanis, J., *ASME J. Fuel Cell Sci. Technol.* **6**, 031015–1–031015-10 (2009).
- Braun, R. J., Kameswaran, S., Yamanis, J. and Sun, E., *J. Eng. Gas Turbines Power* **134**, 021801–1–021801-15 (2012).
- Burke, A. A. and Carreiro, L. G., *J. Power Sources* **158**, 428–435 (2006).
- Carrette, L., Friedrich, K. and Stimming, U., *Fuel Cells* **1**, 5–39 (2001).
- Chen, Y. and Evans, J., *J. Power Sources* **58**, 87–91 (2005).
- Colclasure, A. M., Sanandaji, B. M., Vincent, T. L. and Kee, R. J., *J. Power Sources* **196**, 196–207 (2011).
- Colella, W. G., Schneider, S. H., Kammen, D. M., Jhunjunwala, A. and Teo, N., *ASME J. Fuel Cell Sci. Technol.* **8**, 021001 (2010a).
- Colella, W. G., Schneider, S. H., Kammen, D. M., Jhunjunwala, A. and Teo, N., *ASME J. Fuel Cell Sci. Technol.* **8**, 021002 (2010b).
- Colson, C. M. and Nehrir, M. H., *Energy Convers., IEEE Trans.* **26**, 140–148 (2011).
- Costamagna, P., Arato, E., Achenbach, E. and Reus, U., *J. Power Sources* **52**, 243–249 (1994).
- Costamagna, P., Magistri, L. and Massardo, A., *J. Power Sources* **96**, 352368 (2001).
- Damm, D. L. and Federov, A. G., *J. Power Sources* **159**, 956–967 (2006).
- Duffie, J. A. and Beckman, W. A., *Solar Engineering of Thermal Processes*. 3rd ed. Wiley, New York, NY (2007).
- Erikstrup, N., Jensen, M. D., Nielsen, M. R., Clausen, T. N. and Larsen, P., *ECS Trans.* **25**, 207–212 (2009).
- Fluent software package, Version 13.0, Ansys Inc. see also www.ansys.com.

- Gerdes, K., Grol, E., Keairns, D. and Newby, R., Integrated Gasification Fuel Cell Performance and Cost Assessment. (2009) Technical Report DOE/NETL-2009/1361, National Energy Technology Laboratory, Morgantown, WV.
- Ghosh, D., Performance of Anode Supported Planar SOFC Cells. In "Proceedings of the Sixth International Symposium on SOFCs (SOFC-VI), PV99-19" The Electrochemical Society, Pennington, NJ (1999), p. 822.
- Gong, M., Liu, X., Trembly, J. and Johnson, C., *J. Power Sources* **168**, 289–298 (2007).
- Goodwin, G. C., Graebe, S. F. and Salgado, M. E., Control System Design. Vol. 1, Prentice Hall, New Jersey (2001).
- Gubner, A., Nguyen-Xuan, T., Bram, M., Rimmel, J. and de Hartr, L., European Fuel Cell Forum, Luzern, Switzerland, Paper B042, (2006).
- Hartvigsen, J. J. and Khandkar, A. C., Thermally integrated reformer for solid oxide fuel cells. Number U.S. Patent Number 5,366,819. U.S. Patent Office, Washington, D.C. (1994).
- Hasikos, J., Sarimveis, H., Zervas, P. and Markatos, N., *J. Power Sources* **193**, 258–268 (2009).
- Hawkes, A. D., Aguiar, P., Croxford, B., Leach, M. A., Adjiman, C. S. and Brandon, N. P., *J. Power Sources* **164**, 260–271 (2007).
- Hawkes, A., Staffell, I., Brett, D. and Brandon, N., *Energy Environ. Sci.* **2**, 729–744 (2009).
- Himansu, A., Freeh, J. E., Steffen, C. J., Tornabene, R. T. and Wang, X. J., Hybrid Solid Oxide Fuel Cell/Gas Turbine System Design for High Altitude Long Endurance Aerospace Missions. (2006) Technical Report NASA/TM2006-214328, NASA, Glenn Research Center, Cleveland, OH.
- Huang, B., Qi, Y. and Murshed, M., *Journal of Process Control* **21**, 1426–1437 (2011).
- Huo, H., Zhu, X., Hu, W., Tu, H., Li, J. and Yang, J., *J. Power Sources* **185**, 338–344 (2008).
- Ivers-Tiffée, E., Timmerman, H., Leonide, A., Menzler, N. H. and Malzbender, J., In "Handbook of Fuel Cells-Fundamentals, Technology and Applications" (W. Vielstich, H. Yokokawa and H. A. Gasteiger, Eds.), pp. 933–956. Wiley, Chichester, UK (2009).
- Jurado, F., *J. Power Sources* **158**, 245–253 (2006).
- Kattke, K. J. and Braun, R. J., *J. Power Sources* **196**, 6347–6355 (2011a).
- Kattke, K. J. and Braun, R. J., *ASME J. Fuel Cell Sci. Technol.* **8**, 021009 (2011b).
- Kattke, K. J., Braun, R. J., Coclosure, A. and Goldin, G., *J. Power Sources* **196**, 3790–3802 (2011).
- Kays, W. M. and London, A. L., Compact Heat Exchangers. 3rd ed. Krieger Publishing Company, Malabar, FL (1998).
- Kazempoor, P., Dorer, V. and Weber, A., *Int. J. Hydrogen Energy* **36**, 13241–13249 (2011).
- Kee, R. J., Korada, P., Walters, K. and Pavol, M., *J. Power Sources* **109**, 148–159 (2002).
- Kee, R. J., Almand, B. B., Blasi, J. M., Rosen, B. L., Hartmann, M., Sullivan, N. P., Zhu, H., Manerbino, A. R., Menzer, S., Coors, W. G. and Martin, J. L., *Appl. Thermal Eng.* **31**, 2004–2012 (2011).
- Khandkar, A., Hartvigsen, J. and Elangovan, S., A techno-economic model for SOFC power systems. Proceedings of Solid State Ionics, (2000).
- Larminie, J. and Dicks, A., Fuel Cell Systems—Explained. 2nd ed. Wiley, West Sussex, England (2003).
- Lassiter, R. H., Bulk Power System Dynamics and Control IV: Restructuring Conference Proceedings, Santorini, Greece, (1998).
- Liese, E., *J. Eng. Gas Turbines Power* **132**, 061703 (2010).
- Linderroth, S. and Mogensen, M., Proceedings of the 4th European SOFC Forum, Lucerne, Switzerland, (2000).
- Ljung, L., System Identification: Theory for the User. 2nd ed. Prentice Hall, Upper Saddle River, NJ (1999).
- Lundberg, W. L. Solid oxide fuel cell cogeneration system conceptual design, final report, prepared for the Gas Research Institute GRI, Report No. GRI-89/0162. (1989).
- Massardo, A. F. and Lubelli, F., *J. Eng. Gas Turbines Power* **122**, 27–35 (2000).

- Meusinger, J., Riensche, E. and Stimming, U., *J. Power Sources* **71**, 315–320 (1998).
- Miller, R. M. and Reitz, T. L., In "Advances in Solid Oxide Fuel Cells VI" (P. Singh and N. P. Bansal, Eds.), American Chemical Society, Washington, DC (2010).
- Moran, M. J., Availability Analysis. ASME Press, New York, NY (1989).
- Moran, M. J. and Shapiro, N. N., Fundamentals of Engineering Thermodynamics. 6th ed. Wiley, Hoboken, NJ (2008).
- Morari, M., et al., *Comput. Chem. Eng.* **23**(4–5), 667–682 (1999).
- Mueller, F., Gaynor, R., Auld, A., Brouwer, J., Jabbari, F. and Samuelson, G., *J. Power Sources* **176**, 229–239 (2008).
- Mukerjee, S., Haltiner, K., Klotzbach, D., Vordonis, J., Iyer, A. and Kerr, R., *ECS Trans.* **25**, 59–64 (2009).
- Nanaeda, K., Mueller, F., Brouwer, J. and Samuelson, S., *J. Power Sources* **195**, 3176–3185 (2010).
- Nehter, P., A high fuel utilizing solid oxide fuel cell cycle with regard to the formation of nickel oxide and power density. *J. Power Sources* **164**, 252–259 (2007).
- Palazzi, F., Autissier, N., Marechal, F. M. A. and Favrat, D., *Appl. Thermal Eng.* **27**, 2703–2712 (2007).
- Pillai, M. R., Kim, I., Bierschenk, D. M. and Barnett, S. A., *J. Power Sources* **185**, 1086–1093 (2008).
- Pruitt, K., Newman, A., Leyffer, S. and Braun, R. J., Optimizing the design and dispatch of distributed generation systems for building applications: Modeling approaches. *Optimization and Engineering*, submitted January (2012).
- Pukrushpan, J., Stefanopoulou, A. and Peng, H., Control of Fuel Cell Power Systems: Principles, Modeling, Analysis and Feedback Design. Springer Verlag, New York (2004).
- Qin, S. J. and Badgwell, T. A., *Control Eng. Pract.* **11**(7), 733–764 (2003).
- Riensche, E., Stimming, U. and Unversagt, G., *J. Power Sources* **73**, 251–256 (1998a).
- Riensche, E., Meusinger, J., Stimming, U. and Unversagt, G., *J. Power Sources* **71**, 306–314 (1998b).
- Sarantaridis, D., Rudkin, R. A. and Atkinson, A., Oxidation failure modes of anode-supported solid oxide fuel cells. *J. Power Sources* **180**, 704–710 (2008).
- Sanandaji, B. M., Vincent, T. L., Colclasure, A. M. and Kee, R. J., *J. Power Sources* **196**, 208–217 (2011).
- Sasaki, K. and Teraoka, Y., *J. Electrochem. Soc.* **150**, A878–A888 (2003).
- Schroeder, D. J. and Majumdar, P., *Int. J. Hydrogen Energy* **35**, 11308–11314 (2009).
- Shah, R. K. and Sekulić, D. P., Fundamentals of Heat Exchanger Design. Wiley, Hoboken, NJ (2003).
- Simon, D., Optimal State Estimation: Kalman, H_∞ and Nonlinear Approaches. Wiley-Interscience, Hoboken, NJ (2006).
- Stolten, D., Frohning, D. and deHaart, L. G. J., Proceedings of the fourth European SOFC Forum, Lucerne, Switzerland, July 10–14, (2000).
- Sun, E., Yamanis, J., Chen, L., Frame, D., Holowczak, J., Magdefrau, N., Tulyani, S., Hawkes, J., Haugstetter, C., Radcliff, T. and Tew, D., *ECS Trans.* **25**, 77–84 (2009).
- Szargut, J., Exergy Method Technical and Ecological Applications. WIT Press, Southampton, UK (2005).
- Szargut, J., Morris, D. R. and Stewart, F. R., Exergy Analysis of Thermal, Chemical, and Metallurgical Processes. Hemisphere Publishing, New York, NY (1988).
- Thijssen, J. H., The impact of scale-up and production volume on SOFC manufacturing cost. (2007) Technical report, National Energy Technology Laboratory, Morgantown, WV.
- U.S. Department of Energy Fuel Cells, A Handbook. 7th ed. prepared by EG&G Technical Services, Inc. for the U.S. Department of Energy, Office of Fossil Energy, Morgantown, WV, Contract no. DE-AM26-99FT40575 (2004).

- Van Overschee, P. and De Moor, B., *Subspace Identification for Linear Systems: Theory, Implementation, Applications*. Kluwer Academic Publishers, London (1996).
- Verda, V. and Quaglia, M., *Int. J. Hydrogen Energy* **33**, 2087–2096 (2008).
- Verma, A., Rao, A. D. and Samuelson, G. S., *J. Power Sources* **158**, 417–427 (2006).
- Veyo, S., *Proceedings of IEEE*, pp. 1138–1143. (1996).
- Wagner, E. S. and Froment, G. F., *Hydrocarbon Process.* **7**, 69–77 (1992).
- Wang, J., *Int. J. Hydrogen Energy* **33**, 6339–6350 (2008).
- Wang, J., *Chem. Eng. J.* **168**, 1131–1345 (2011).
- Wang, Y. and Boyd, S., *IEEE Trans. Control Syst. Technol.* **18**(2), 267–278 (2010).
- Wark, K., *Advanced Engineering Thermodynamics*. 2nd ed. McGraw-Hill, New York, NY (1995).
- Yang, J. S., Sohn, J. L. and Ro, J., *J. Power Sources* **166**, 155–164 (2007).
- Yang, L., Wang, S., Blinn, K., Liu, M., Liu, Z., Cheng, Z. and Liu, M., *Science* **326**, 126–129 (2009a).
- Yang, J., Li, X., Mou, H. and Jian, L., *J. Power Sources* **188**, 475–482 (2009b).
- Yang, J., Li, X., Mou, H. and Jian, L., *J. Power Sources* **193**, 699–705 (2009c).
- Yi, Y., Rao, A., Brouwer, J. and Samuelson, G. S., *J. Power Sources* **144**, 67–76 (2005).
- Zha, S., Cheng, Z. and Liu, M., *J. Electrochem. Soc.* **154**, B201–B206 (2007).